Du transport de particules à l'optimisation globale sous contrainte d'équations aux dérivées partielles

Laurent Dumas

Université Pierre et Marie Curie

Laboratoire Jacques-Louis Lions

Mémoire présenté en vue d'une

Habilitation à Diriger des Recherches

Spécialité : Mathématiques Appliquées

soutenue le **3 décembre 2008**

par : **Laurent DUMAS**

Du transport de particules à l'optimisation globale sous contrainte d'équations aux dérivées partielles

(ou une approche des mathématiques en vue de ses applications industrielles et médicales)

Composition du jury

Rapporteurs

François Dubois (Conservatoire National des Arts et Métiers, Paris)
Pekka Neittaanmäki (University of Jyväskylä, Finland)
Marc Schoenauer (INRIA Saclay)

Examinateurs

Frédéric Hecht (Université Pierre et Marie Curie)
Mohamed Masmoudi (Université Toulouse III)
Bijan Mohammadi (Université Montpellier II)
Benoit Perthame (Université Pierre et Marie Curie)
Olivier Pironneau (Université Pierre et Marie Curie)

Remerciements

Comme le sous-titre de ce mémoire l'indique, mon parcours scientifique depuis ma thèse, loin d'être linéaire, aura été guidé avant tout par le goût des applications des mathématiques découvert lors d'un stage à l'Aérospatiale en 1992. Plutôt que de poursuivre dans la voie des équations cinétiques, j'ai donc choisi, tel une particule dans un billard périodique, d'aller découvrir de nouveaux sujets mathématiques au gré des applications industrielles ou médicales rencontrées. Néanmoins, je tiens ici à adresser mes premiers remerciements à Claude Bardos et François Golse pour m'avoir formé à l'école de la rigueur mathématique.

Je remercie François Dubois, Pekka Neittaanmäki et Marc Schoenauer qui ont accepté la tâche de rapporteur. Ils ont également eu l'extrême gentillesse de le faire dans des délais m'autorisant à soutenir en 2008. Qu'ils soient ici remerciés pour tout cela.

Je souhaite ensuite remercier Olivier Pironneau qui m'a depuis de nombreuses années toujours encouragé à poursuivre dans la voie que j'avais choisie et m'a aidé à déjouer ses nombreux pièges. Il est pour moi un modèle scientifique mais aussi humain.

Après avoir regardé du coté des fusées, des voitures, des avions ou des prothèses en silicones, j'ai eu l'envie de donner un sens moins matériel à ma recherche en me plongeant dans les applications médicales. La rencontre avec Jean Frédéric Gerbeau à ce stade a été décisive. Son enthousiasme scientifique, sa vision du domaine sont toujours pour moi un régal à partager.

J'ai eu le plaisir de rencontrer il y a quelques années au Vietnam, un vétéran de l'aviation (coté simulations !), non pas John Mac Cain mais Bijan Mohammadi. Je me régale de nos discussions sur tous les sujets chaque fois que nos chemins se recroisent. Je suis très honoré qu'il ait accepté de participer à mon jury. Je suis très honoré également que Frédéric Hecht, Mohamed Masmoudi et Benoit Perthame soient membres de mon jury. Benoit était en particulier déjà présent lors de ma thèse. Même si je n'ai peut être pas atteint les attentes qu'il plaçait en moi à ce moment ou au cours de mon parcours, sa présence à mon jury me pousse à poursuivre dans ce sens.

Inévitablement, en écrivant ces remerciements, j'ai été amené à me replonger dans ceux écrits pour ma thèse. C'était il y a 13 ans, un siècle, une éternité ! Cependant, outre pas mal de points communs dans mes goûts scientifiques, j'y retrouve un certain nombre d'amitiés jamais démenties et dont j'eus bien besoin parfois, je pense à Pascal, Raphaël et Max. D'autres sont apparues au détour des couloirs de Chevaleret comme celles d'Adel, Tahar, Driss, Frédéric, Kaber, Sergio, Christophe, Franck bien luné, Valéria, Alexandra.

Comme 13 ans plus tôt, je remercie ma soeur pour m'avoir balisé le chemin des études ainsi que mon papa toujours disponible malgré son agenda de ministre. Mon seul regret est que je ne puisse pas profiter de ses relations pour un billet de match de temps en temps ou même pour pouvoir entrer au village étape du Tour de France... En fait, la seule relation dont je profite abondamment grâce à lui et avec plaisir est celle de Thérèse et sa délicieuse cuisine.

Ma maman n'est hélas plus de ce monde mais je sais que de l'endroit où elle est, elle sera heureuse de nous voir tous réunis. Je lui dédie ce mémoire qui lui doit tant.

De toutes les rencontres, la plus importante n'est en fait pas scientifique mais celle que j'ai faite avec ma chérie Djamila. Sa générosité, sa grandeur d'âme et son accent anglais sont un exemple pour moi. Elle m'a même fait aimer Thiais, Bryan Ferry et les poivrons, c'est dire...

Pour finir, j'embrasse très fort mon petit boubou Elias qui vient de naître (vive l'année 2008 !) ainsi que mon petit coco Nicolas. Vous êtes les deux fils dont j'ai toujours rêvé. La vie promet d'être belle avec vous encore très longtemps.

Table des matières

Publications

1. Livre :

[L1] L. Dumas, Modélisation à l'oral de l'Agrégation, calcul scientifique, Ellipse (1999).

2. Chapitre de livre :

[Cha1] L. Dumas, 'CFD-based optimisation in Automotive Aerodynamics' in '*Optimization in Computational Fluid Dynamics*', D. Thévenin, G. Janiga editors, Springer, p. 191-215 (2008).

3. Articles :

3.1 Transport de particules

[Art1] L. Dumas, H.S. Dumas, F. Golse, On the mean free path for a periodic array of spherical obstacles,*Journal of Statistical Physics*, Vol 82, n°5-6, p. 1385-1407 (1996).
[Art2] C. Bardos, L. Dumas, F. Golse Diffusion approximation for billiards with totally accomodating scatterers, *Journal of Statistical Physics*, Vol 86, n°1-2, p. 351-375 (1997).
[Art3] L. Dumas, H.S. Dumas, F. Golse, Remarks on the notion of mean free path for a periodic array of spherical obstacles,*Journal of Statistical Physics*, Vol 87, n° 3-4, p. 943-950 (1997).
[Art4] L. Dumas, F. Golse, Homogenization of transport equations, *SIAM Journal of Applied Mathematics*, Vol. 60, no 4, p. 1447-1470 (2000).

3.2 Optimisation et applications pour l'automobile

[Art5] L. Dumas, V. Herbert, F. Muyl, Hybrid method for aerodynamic shape optimization in automotive industry., *Computers and Fluids*, Vol. 33, p. 849-858 (2004).
[Art6] L. Dumas, V. Herbert, F. Muyl, Comparison of global optimization methods for drag reduction in the automotive industry, *Lecture Notes in Computer Science*, Vol. 3483, p. 948-957 (2005).
[Art7] L. Dumas, V. Herbert, F. Muyl, Optimisation de forme en aérodynamique automobile, *Mécanique et Industrie*, EDP Sciences, Vol. 6 no. 3, p. 285-288 (2005).

3.3 Optimisation et applications pour les télécommunications

[Art8] L. Dumas, O. Durand, B. Ivorra, B. Mohammadi, Semi-deteministic method recursive optimization methods for multichannel optical filters, *Numerical mathematics and advanced applications*, p. 1007-1014, Springer, Berlin (2006).
[Art9] L. Dumas, O. Durand, B. Ivorra, B. Mohammadi, P. Redont, Semi deterministic vs Genetic Algorithms for global optimization of multichannel optical filters, *International Journal of Computational Science and Engineering*, Vol.2, p. 170-178 (2006).

3.4 Optimisation et applications aéronautiques

[Art10] B. Druez, L. Dumas, N. Lecerf, Adaptive Hybrid Optimization of aircraft engine blades, accepté dans *Journal of Computational and Applied Mathematics* (2008).

3.5 Optimisation et applications médicales

[Art11] L. Dumas, Inverse problems for the simulation of blood flow in arteries, soumis à *Inverse Problems in Science and Engineering.*
[Art12] L. Dumas, L. El Alaoui, M. Fernandez, J.F. Gerbeau, Optimal positioning of electrodes for a pacemaker : a numerical model, *en cours de rédaction.*

4. Conférences internationales avec proceedings

4.1 Transport de particules et applications aux propulseurs de fusées

[Proc1] J.F. Chauvot, L. Dumas, K. Schmeisser, Modeling of slag deposition in solid rocket motors, *31th AIAA Joint Propulsion conference*, San Diego, n° 95/2729 (1995).
[Proc2] N. Cesco, L. Dumas, A. Hulin, T. Pevergne, Y. Fabignon Stochastic models to the investigation of slag accumulation in a large solid rocket motor, *33rd AIAA/ASME/SAE/ASEE Joint Propulsion Conference*, Seattle, n°97/3118 (1997).

4.2 Optimisation et applications médicales

[Proc3] L. Dumas, L. El Alaoui, Application of Genetic Algorithms to cure heartbeat pathologies, *proceedings of EUROGEN* (2007).
[Proc4] L. Dumas, L. El Alaoui, How Genetic Algorithms can improve a pacemaker efficiency, *proceedings of GECCO 2007*, p. 2681-2686 (2007).
[Proc5] A. Blouza, L. Dumas, I. M'Baye, Multi Objective Optimization of a Stent in a Fluid-Structure Context, *proceedings of GECCO 2008*, p. 2056-2060 (2008).
[Proc6] L. Dumas, An Inverse Problem in Blood Flow Simulation, *proceedings of ENGOPT* (2008).

5. Conférences nationales avec proceedings

5.1 Transport de particules et applications aux propulseurs de fusées

[Conf1] P. Belomi, L. Dumas, Y. Fabignon, L. Jacques, G. Lavergne, Prévision du dépôt d'alumine dans les moteurs à propergol solide, 5ème symposium internationale sur la propulsion dans les transports spatiaux (1995).

6. Rapport technique

[Rap1] L. Dumas, Modélisation de la déformation des polymères solides, rapport interne RHODIA (2000).

Résumé

Pour bien comprendre les orientations suivies dans ce mémoire, il convient de replacer les travaux présentés dans leur contexte historique. Au commencement de ce travail, au milieu des années 90, il y eut le projet de navette européenne Hermès et les problèmes associés de réentrée dans la haute atmosphère qui m'orientèrent vers l'étude des modèles cinétiques et leurs simulations numériques par les méthodes de type Monte Carlo. Malheureusement, le lancement de la fusée Ariane 5, réalisé en 1997, est à ce jour le dernier grand projet spatial européen. A la fin des années 90, avec l'essor des moyens informatiques, de nouvelles perspectives virent le jour dans les bureaux d'études d'ingénieurs : la possibilité de lancer une boucle d'optimisation en arrière plan de simulations complexes 3D : cette nouvelle voie me redirigea alors vers l'étude et l'amélioration des méthodes d'optimisation de type Algorithmes Génétiques pour toutes sortes d'applications : optimisation du Cx d'automobiles, optimisation du rendement de réacteurs d'avions, etc... Le même type de problèmes d'optimisation s'est ensuite retrouvé dans le domaine médical et a attiré mon attention depuis mon intégration au sein de l'équipe REO en 2004 : optimisation de dispositifs médicaux comme les stents ou les pacemakers, identification de paramètres de modèles numériques d'écoulements sanguins.

La première partie de ce mémoire est consacrée à des travaux sur le transport de particules dans le prolongement de ma thèse soutenue en 1995 : étude du libre parcours moyen de particules dans un réseau d'obstacles périodiques, trajectoires de particules dans un écoulement fluide turbulent. L'application visée dans cette dernière étude consistait à estimer le dépôt d'alumine dans le fond arrière du propulseur à poudre de la fusée Ariane 5. La seconde partie consiste en la présentation des méthodes d'optimisation hybrides et des principes d'évaluations approchées ayant permis d'améliorer les performances des méthodes de type Algorithmes Génétiques. La troisième partie présente un certain nombre d'application des méthodes précédentes à des problèmes d'optimisation ayant pour point commun leur caractère global ainsi que la présence de contraintes s'exprimant sous la forme d'EDO ou d'EDP. Chacun de ces problèmes est par ailleurs issu d'une problématique d'ingénierie ou médicale.

1. Transport de particules dans diverses configurations

Le transport de particules a été étudié dans deux configurations particulières. Chacune d'elles est directement ou indirectement liée à deux applications aérospatiales que j'ai eu l'occasion d'aborder lors de mes 3 années d'ingénieur à EADS (ex-Aérospatiale), respectivement la réentrée de la navette Hermès et le dépôt d'alumine dans les boosters d'Ariane 5.

La première configuration consiste en l'étude de particules ponctuelles se déplaçant dans un réseau périodique d'obstacles dans $\mathbb{R}^n$. Ce modèle, parfois appelé gaz de Lorentz ou billard de Sinai, est un premier pas vers l'étude de l'équation de Boltzman régissant les écoulements dans la haute atmosphère. La série d'articles [Art1], [Art2] et [Art3] réalisée dans le prolongement de ma thèse soutenue en 1995, étudie le comportement asymptotique de ce modèle en fonction de la taille respective r des obstacles par rapport à leur distance mutuelle a. Dans le cas où ce rapport est constant et que r et a tendent vers 0, il est démontré dans [Art2] que le comportement limite en temps grand d'un tel système est régi par une équation de diffusion. Les articles [Art1] et [Art3] s'intéressent pour leur part à étudier le modèle lorsque r est de l'ordre de a^γ avec $\gamma > 1$. L'introduction de la notion de libre parcours moyen des particules permet de dissocier les différents cas observés en fonction de γ. Un exposant critique $\gamma_c = \frac{n}{n-1}$ est en particulier exhibé séparant les situations où le libre parcours moyen tend vers 0 ou l'infini. A noter que l'article [Art4] s'intéresse à une problématique de transport légèrement différente, à savoir l'étude asymptotique des équations de transport par homogénéisation lorsque les sections efficaces de collision ont des ordres de grandeur très différents à petite échelle.

La deuxième configuration, encore plus proche de l'application industrielle, consiste en l'étude générale des trajectoires de particules (solides ou liquides) dans un fluide turbulent dans le but d'estimer le dépôt d'alumine dans le fond arrière des propulseurs à poudre d'Ariane 5. Sur les 230 tonnes de propergol contenues initialement dans chaque booster, des test expérimentaux ont en effet mis en évidence la présence d'environ 2 tonnes de dépôt d'alumine en fin de poussée pouvant alors mettre en danger la stabilité du lanceur. Le modèle numérique présenté dans [Proc1], [Proc2] et [Conf1] est basé sur une simulation stationnaire de l'écoulement à différents instants dans la chambre de combustion et en l'étude des trajectoires des particules d'alumine issues du bloc en combustion. La turbulence du fluide est prise en compte dans le modèle par l'adjonction dans la vitesse des particules d'une perturbation gaussienne. Les résultats ont permis de retrouver des valeurs parfaitement réalistes de dépôt et ont également mis en évidence l'importance du terme stochastique dans le modèle.

2. Méthodes d'optimisation globale

Un nouveau challenge numérique a vu le jour à la fin des années 90 dans un nombre très varié de secteurs de l'industrie, à savoir l'optimisation de formes de divers objets (automobile, avion, etc..) dont la simulation directe nécessite déjà des calculs coûteux. C'est au travers de différentes collaborations industrielles (PSA, Alcatel et Safran principalement) que je suis arrivé naturellement à m'intéresser à ce sujet transversal.

En termes mathématiques, l'objectif consiste à rechercher le minimum global d'une fonction réelle J définie sur un sous ensemble $\mathcal{O}$ de $\mathbb{R}^n$. En raison de la complexité du principe d'évaluation de cette fonction, souvent issue de la résolution d'une EDO ou d'une EDP dans une géométrie complexe, le recours aux méthode d'optimisation stochastiques évolutionaires (Algorithmes Génétiques, Stratégies d'Evolution, PSO, etc...) s'avère souvent inévitable.

Pour les problèmes les plus coûteux, comme par exemple l'optimisation du Cx d'une automobile nécessitant une simulation tridimensionnelle des équations de Navier Stokes, le développement de principes d'accélération de convergence des méthodes évolutionaires classiques a été également nécessaire. Deux axes ont plus particulièrement été étudiés : la première idée consiste à coupler les méthodes évolutionaires (AG, ES) avec des méthodes d'optimisation déterministes locales comme les méthodes de gradient. Après différents essais sur la bonne stratégie de couplage amorcés dès 2002 dans [Art5], [Art6] et [Art7], un couplage totalement adaptatif est proposé dans [Art10]. Il consiste à choisir les instants de transition entre la recherche globale et la recherche locale en fonction de critères généraux de répartition de la population de solutions et à subdiviser celle-ci pour répartir plus efficacement les recherches locales. Avec une telle stratégie et pour les cas les plus défavorables de fonctions ayant un grand nombre de minima locaux, le gain en termes d'évaluations de J entre une telle méthode dite hybride et une méthode classique se situe aux alentours d'un facteur trois. Un deuxième axe de recherche pour accélérer les méthodes évolutionaires consiste à développer des modèles d'évaluations approchées à partir d'un échantillon d'évaluation exactes de la fonction coût J. Un nouveau modèle a été proposé dans [Art6] basé sur des méthodes d'approximation de type RBF et la résolution d'un problème aux moindres carrés. Une version simplifiée de ce modèle ayant permis d'observer également un gain important et reproductible est utilisée dans [Art12] et présentée dans le paragraphe 2.3.

Ces deux types d'améliorations, appelées respectivement tout au long de ce travail AHM (Adaptive Hybrid Method) et AGA (Approximate Genetic Algorithm) ont été largement validées dans chacune des références citées sur des fonctions analytiques reproduisant différentes caractéristiques de fonctions réalistes (nombreux minimas locaux, bassins d'attraction étroits ou quasi-plats, etc...).

3. Optimisation globale sous contrainte d'EDO ou d'EDP : applications

Différentes applications, six au total, des méthodes précédentes sont présentées dans ce chapitre. Toutes sont issues de problèmes applicatifs, trois le domaine des sciences de l'ingénieur, trois dans le domaine médical. Dans chacun des cas, la résolution du problème direct a nécessité une étude préalable approfondie et parfois le développement de nouveaux modèles. De même, pour certaines applications, le choix de la fonction coût et de la paramétrisation du problème se sont avérés déterminants.

La section 3.1 présente la modélisation et la simulation d'un problème inverse soumis par Alcatel dans le but de construire des fibres optiques particulières, appelées réseaux de Bragg (FBG). Les simulations détaillées dans [Art8] et [Art9] permettent d'obtenir des résultats très satisfaisants, aussi bien avec des méthodes de type Algorithmes Génétiques qu'avec une méthode semi-déterministe développée par B. Mohammadi. Le principal intérêt des résultats obtenus, comparativement à d'autres méthodes précédemment utilisées, réside dans la facilité de réalisation expérimentale des fibres optimales numériquement exhibées.

La section 3.2 s'intéresse à un problème inverse à fortes applications médicales potentielles. Il s'agit d'identifier de manière expérimentale les paramètres d'un modèle monodimensionnel d'écoulement sanguin. Par rapport à des résultats antérieurs obtenus par J.F. Gerbeau et al. pour des artères à flexibilité constante, le travail a consisté à développer et à valider un modèle numérique d'écoulement dans des artères avec flexibilité variable, afin de simuler par exemple la présence de plaques d'athérome. Les résultats obtenus, présentés dans [Proc6] et [Art11], montrent par exemple qu'il est possible de reconstruire un modèle simple et pertinent seulement à partir de mesures expérimentales non invasives en aval de la plaque d'athérome.

La section 3.3 présente les résultats d'une collaboration de 5 ans avec le constructeur automobile Peugeot Citroën PSA, incluant en particulier l'encadrement d'une étudiante en thèse Cifre (F. Muyl). L'objectif fixé dès 1999 était de développer des outils automatiques d'optimisation de formes de véhicules dans le but crucial de réduire leur consommation. Au vu de la complexité de l'évaluation de la fonction coût correspondante (le Cx du véhicule), l'accent a été mis dans cette collaboration sur l'accélération de convergence des méthodes de type Algorithmes Génétiques, soit par hybridation avec des méthodes de gradient, soit à l'aide d'évaluations approchées. Les résultats, présentés dans [Cha1], [Art5], [Art6], [Art7] ont été tous validés sur une forme expérimentale inspirée du bluff body d'Ahmed.

La section 3.4 est consacrée à l'amélioration du fonctionnement d'un pacemaker en recherchant les instants et les positionnements idéaux de ses électrodes. Ces travaux, effectués dans le cadre du projet REO ont donné lieu à l'encadrement en 2007 d'une étudiante en post-Docorat (L. El Alaoui). Après la mise au point de la résolution du problème direct ainsi qu'une réflexion sur la fonction coût la plus pertinente, les premiers résultats présentés dans [Proc4] et en cours de rédaction dans [Art12] ont mis en évidence le gain important pouvant être obtenu en optimisant le placement des électrodes. A noter que la lourdeur du calcul direct a nécessité l'usage des méthodes de type AGA pour obtenir les solutions optimales en un temps de calcul raisonnable.

Enfin, la sections 3.5 présente deux autres exemples d'optimisation dans des domaines applicatifs, en l'occurrence l'optimisation multi-objectifs de la formes de stents (voir [Proc6] pour plus de détails) et l'optimisation avec la méthode AHM de la formes d'aubes de turboréacteurs d'avions (travaux réalisés conjointement avec Safran et présentés dans [Cha1] et [Art10]).

N.B. : A partir ce de point, l'auteur tient à préciser que le reste du mémoire a été rédigé en anglais et s'en excuse d'avance auprès des défenseurs de la langue de Molière...

Summary

In order to understand the evolution of this work throughout the years, some historical explanations are needed. At the beginning of this work, in the mid-90's, the Hermes project and its associated reentry problem, lead me to study kinetic models and their corresponding numerical simulations with the Monte Carlo method. Unfortunately, the Ariane 5 firing in 1997 is up to now the last large European space project. At the end of this decade, with the growing computational ability, a new perspective opened for engineers : the possibility to do an optimization loop even with complex 3D simulations. This new challenge brought me to the field of evolutionary algorithms in order to try to apply and eventually improve them for various problems : car shape optimization, turbine blade shape optimization etc... The same kind of problems appeared later in the medical field in which I work since 2004 and my integration inside the REO team : optimization of medical devices like stents or pacemakers, parameters identification of numerical blood flow models, etc...

The first part of this document is devoted to my work on particles transport after my PhD defence in 1995 : asymptotic behavior of the particles mean free path in a periodic array of scatterers, particles trajectories in a turbulent fluid. The application at stake for this last point was the numerical simulation of slag deposition at the motor case walls of the Ariane 5 boosters. The second part of this document deals with the description of hybrid optimization methods and surrogate models developed in order to improve the performance of evolutionary algorithms. Finally, the third and last part gives various applications of the previous optimization methods to applicative fields, coming either from industry or medicine, and having all ODE or PDE constraints.

1. Particles trajectories in various configurations

Two distinct configurations including particles trajectories computations have been studied. Both are linked, more or less, to two applicative problems I have encountered during my three years as research engineer at EADS (ex-Aerospatiale), respectively the Hermes space shuttle reentry problem and the slag deposition problem in the Ariane 5 boosters.

The first configuration consists in studying the trajectories of point particles moving in a periodic array of circular obstacles of $\mathbb{R}^n$. This model, also called Lorentz gas or Sinai billiard, is a first step in the study of the Boltzman equation describing the evolution of rarefied gases. The three articles [Art1], [Art2] et [Art3] written in the continuity of my PhD defence in 1995, study the asymptotic behavior of such systems with respect to the size of obstacles r and their mutual distance a. In the case where r and a go to 0 simultaneously with a constant rate, it is proven in [Art2] that for large time, the model satisifies a diffusion equation in $\mathbb{R}^n$. The articles [Art1] and [Art3] are devoted to the asymptotic study of the Lorentz gas where r is of the order of a^γ with $\gamma > 1$. The introduction of the notion of mean free path allows to study the behavior of the particles depending on γ. A critical value $\gamma_c = \frac{n}{n-1}$ is in particular introduced, separating the cases where the mean free path goes to zero, respectively diverges to infinity. Note that [Art4] is studying a slightly different linear transport model in which the transport cross section is rapidly varying at small space scales. An equivalent model is then deduced by using homogenization techniques.

The second configuration, more close to the real application, corresponds to the study of point particles trajectories (solid or liquid) immersed in a turbulent gas. The objective is here to estimate numerically the amount of slag deposition at the motor case walls of the Ariane 5 boosters. Indeed, a slag deposition approximately equal to 2 tons (compared to the initial 230 tons of propellant) has been measured of the end of the boosters flight, that could endanger the launcher stability. The numerical model presented in [Proc1], [Proc2] and [Conf1] is based on a

steady state simulation at various burning times of the combustion chamber flow associated to a Lagrangian particles tracking routine. The flow turbulence is taken into account in the model by adding a normal random perturbation to the particles velocity. This model has allowed to recover a correct order of magnitude of slag deposition. In these results, the stochastic term in the particle velocity plays a crucial role.

2. Global optimization methods

A new numerical challenge broke through at the end of the 90's in various industrial field : the opportunity to make shape optimization of various bodies (cars, planes, etc...) fort which the direct simulation is already costly. I came to this transverse field through several collaborations with industrial partners (mainly PSA, Alcatel and Safran).

Mathematically speaking, the objective is to seek for the global minimum of a real cost function J defined on a subset $\mathcal{O}$ of $\mathbb{R}^n$. Because of the complexity of the direct evaluation principle often issued from an ODE or a PDE simulation in complex geometries, the use of evolutionary algorithms (Genetic Algorithms, Evolution Strategies, PSO,...) is necessary in most cases.

For the most costly problems, like for instance the car shape optimization issued from a 3d Navier Stokes simulation, a convergence acceleration principle for evolutionary algorithms is almost mandatory. To this aim, two distinct improvements have been studied. The first idea is to couple evolutionary algorithms with deterministic local search methods like gradient methods. After various attempts started since 2002 in [Art5], [Art6] and [Art7] a fully adaptive coupling is proposed in [Art10]. It consists in selecting the transition shifts between the global and the local search with some criterions based on the repartition of the population and to divide the latter into subpopulations to extend as much as possible the local search exploration. With such a strategy, the gain between this hybrid method and a classical method ranges up to a factor three even for analytic functions exhibiting a large number of local minima. A second improvement concerns the introduction of surrogate models based on the computation of an approximation of the cost function using the database of exact evaluations of J already made. A new model has been proposed in [Art6] and [Art7] based on an RBF interpolation and a least square resolution problem. A simplified version of this model leading also to a very reproducible and important gain is presented in [Art12] and in section 2.3.

These two kinds of improvement, called throughout this work AHM (Adaptive Hybrid Method) and AGA (Approximate Genetic Algorithm) have been validated on analytic functions exhibiting various characteristics of real ones (local minima, steep or quasi-flat attraction basins, ...).

3. Global optimization with ODE or PDE constraints : applicative examples

Various applications, namely six, of the previous optimization methods are presented in this chapter. All are issued from applicative fields, three in engineering science and three in medicine. In all six cases, the direct problem has first needed a deep investigation and sometimes the development of new models. As well, the choice for the cost function and for the problem parametrization have been particulary emphasized.

Section 3.1 presents the modelization and the simulation of an inverse problem that has been suggested by Alcatel in order to build a particular class of optical fibers, namely Fiber Bragg Gratings (FBG). The results detailed in [Art8] and [Art9] are very satisfactory, either by using a Genetic Algorithm or a semi-deterministic method developed by B. Mohammadi. One of the

major interest of these results, compared to those obtained by the method previously used, lies in their simplicity in view of an experimental implementation.

Section 3.2 focuses to an inverse problem with high potential applications in medicine. It consists in experimentally identifying the parameters of a simple blood flow model through arteries. Compared to other results previously obtained by J.F. Gerbeau et al. for arteries with a fixed compliance, the same problem has been studied for arteries with a variable compliance, in order to simulate various phenomenons (atherosclerosis, stented arteries). The results presented in [Proc6] and [Art11] show for instance that it is possible to recover a simple and accurate model only by measuring non invasive quantities downstream the atherosclerosis plaque.

Section 3.3 presents the results of a 5 years collaboration with the French car manufacturer Peugeot Citroën PSA, including a PhD program through a Cifre contract (F. Muyl). The aim, fixed in 1999, was to develop automatic tools for car shape optimization in order to reduce their fuel consumption. In view of the complexity of the cost function evaluation (the car drag coefficient), the emphasis has been made on the construction of convergence acceleration principles of Genetic Algorithms, either by using a coupling with gradient based methods or by developing surrogate models. The results, presented in [Art5], [Art6] and [Art7] have been validated on an experimental car shape inspired from the Ahmed bluff body.

Section 3.4 is devoted to the improvement of a pacemaker by seeking for the optimal positioning and stimulation time of its associated electrodes. This work, made in the context of the REO team has involved in 2007 a post doc program (L. El Alaoui). After the correct setting of the direct problem and a discussion on the most pertinent cost function, the first results presented in [Proc4] and to appear in [Art12] have shown the important gain that can be achieved by optimizing the electrodes positioning. Note that because of the computational cost of the direct problem, an AGA method has been used.

Finally, section 3.5 ends with two other applicative optimization problems, namely the multi-objective optimization of stent shapes (see [Proc6] for more details) and the turbine blade shape optimization with the AHM method (joint work with Safran, detailed in [Cha1] and [Art10]).

Chapitre 1
Particles trajectories in various configurations

1.1 Particles trajectories in a periodic array of scatterers

Summary. The trajectories of point particles moving in a periodic array of circular obstacles are studied in the asymptotic limit where the obstacles are small but very near. Two definitions of the mean free path of particles, respectively designed as geometric and mean truncated free path, are proposed and asymptotically studied. In both cases, convergence results are given depending on the ratio between the size of the obstacles and their distance.

References : [Art1], [Art3].

1.1.1 The Lorentz gas

One family of simplified models that has played an important role in statistical mechanics and kinetic theory is the so-called Lorentz gas in a plane dispersive billiard consisting of a periodic array of circular obstacles, together with its higher dimensional analogues (see Figure 1.1 and [2, 3, 4, 5, 6, 7, 8, 9, 10, 11, 12]).

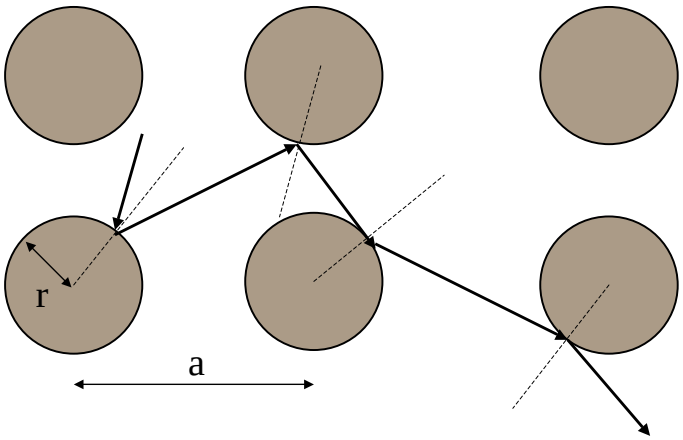

Fig. 1.1 The Lorentz gas

In kinetic theory, it is particularly interesting to study the behavior of particles in such billiards in the macroscopic limit (i.e., as the size of the array is reduced to zero). Let $r \in]0,1/2[$ and $\gamma \geq 1$; for all $\varepsilon \in]0,1[$, let

$$Z_\varepsilon = \{x \in \mathbb{R}^n \mid \text{ dist}(x, \varepsilon\mathbb{Z}) > r\varepsilon^\gamma\}$$

and $Y_\varepsilon = Z_\varepsilon/\varepsilon\mathbb{Z}^n$.

The "length of free path" starting from point $x \in Z_\varepsilon$ in direction $-\omega \in S^{n-1}$ is the nonnegative borelian function

$$\tau_\varepsilon(\cdot,\cdot;\gamma) : \quad Y_\varepsilon \times S^{n-1} \to \mathbb{R}^+$$

defined by the formula :

$$\tau_\varepsilon(x,\omega;\gamma) = \inf\{t > 0 \,|\, x - t\omega \in \partial Z_\varepsilon\} = \sup\{t \geq 0 \,|\, [x, x - t\omega] \subset \overline{Z}_\varepsilon\}$$

There are two different, natural probability measures on $Y_\varepsilon \times S^{n-1}$ with respect to which τ_ε can be studied as a random variable. One is the normalized Lebesgue measure on $Y_\varepsilon \times S^{n-1}$:

$$\mu_{\varepsilon,\gamma} = Q_\varepsilon^{-1} dx d\omega\,, \qquad Q_\varepsilon = dx d\omega - \text{meas } (Y_\varepsilon \times S^{n-1})$$

The other is the normalized measure concentrated on

$$\Sigma_\varepsilon^+ = \{(x,\omega) \in (\partial Z_\varepsilon \cap Y_\varepsilon) \cap S^{n-1} \,|\, \omega \cdot n_x > 0\}$$

where n_x is the inward unit normal at point $x \in \partial Z_\varepsilon$ defined by

$$\nu_{\varepsilon,\gamma} = \Gamma_\varepsilon^{-1} dS(x) d\omega\,, \qquad G_\varepsilon = dS(x) d\omega - \text{meas } (\Sigma_\varepsilon^+)$$

Both these probability measures are invariant under the evolution of the Lorentz gas. The measure $\mu_{\varepsilon,\gamma}$ is invariant under the broken flow on $Z_\varepsilon \times S^{n-1}$ associated to

$$\frac{dx}{dt} = \omega\,, \quad \frac{d\omega}{dt} = 0\,, \quad \text{ whenever } x \notin \partial Z_\varepsilon\,;$$

$$x(t_0{+}0) = x(t_0{-}0)\,, \quad \omega(t_0{+}0) = \omega(t_0{-}0) - 2\omega(t_0{-}0)\cdot n_{x(t_0-0)}\, n_{x(t_0-0)}, \quad \text{ whenever } x(t_0) \in \partial Z_\varepsilon.$$

The measure $\nu_{\varepsilon,\gamma}$ is invariant under the map $\Sigma_\varepsilon^+ \to \Sigma_\varepsilon^+$ defined a.e. by

$$(x,\omega) \mapsto (x' = x + \tau_\varepsilon(x, -\omega;\gamma)\omega; \omega' = \omega - 2\omega \cdot n_{x'}\, n_{x'}) \tag{1.1}$$

We shall denote by $\phi_{\varepsilon,\gamma}$ and $\psi_{\varepsilon,\gamma}$ respectively the push-forward of the measures $\mu_{\varepsilon,\gamma}$ and $\nu_{\varepsilon,\gamma}$ under $\tau(\cdot,\cdot;\gamma)$; in other words, $\phi_{\varepsilon,\gamma}$ and $\psi_{\varepsilon,\gamma}$ are the probability measures on $\mathbb{R}^+$ such that

$$\phi_{\varepsilon,\gamma}(A) = \mu_{\varepsilon,\gamma}(\tau_\varepsilon(\cdot,\cdot;\gamma)^{-1}(A))\,, \quad \psi_{\varepsilon,\gamma}(A) = \nu_{\varepsilon,\gamma}(\tau_\varepsilon(\cdot,\cdot;\gamma)^{-1}(A))\,,$$

for all measurable subset A of $\mathbb{R}^+$.

1.1.2 Two definitions of mean free path

There are two possible notions of mean free path associated to the periodic Lorentz gas in Z_ε :

$$\lambda(\varepsilon,\gamma) = \int_0^{+\infty} z\, d\phi_{\varepsilon,\gamma}(z) \tag{1.2}$$

and for all $T > 0$

$$l(\varepsilon, T, \gamma) = \int_0^{+\infty} \inf(z, T) d\psi_{\varepsilon,\gamma}(z) \tag{1.3}$$

The first one, $\lambda(\varepsilon, \gamma)$ will be referred to as the "geometric mean free path", the second one $l(\varepsilon, T, \gamma)$ as the "mean truncated free path". The truncation in the second definition is necessary because it can be proven that $l(\varepsilon, +\infty, \gamma) = +\infty$. This is why we shall refrain from calling $l(\varepsilon, T, \gamma)$ the mean free path.

The same construction applies to the most general" billiard tables" (see [5, 9]). Whenever the analogue of the map (1.1) is ergodic for the measure $\nu_{\varepsilon,\gamma}$, the geometric mean free path can be interpreted as the average path between N successive collisions of a point particle on the obstacles (the boundary of Z_ε) with specular reflections at the boundary of each obstacle, in the limit as $N \to +\infty$. This follows immediately from the Birkhoff ergodic theorem and is the reason why the geometric mean free path is considered as a natural quantity associated to billiards (see [5, 9]).

However, if one is interested in the evolution of a population of point particles undergoing collisions only with the boundary of Z_ε, the mean truncated free path is a more natural quantity.

1.1.3 Asymptotic results on the mean free path

First, the geometric mean free path can be computed explicitly (see for example [5], §4) :

$$\lambda(\varepsilon, \gamma) = \frac{Q_\varepsilon}{\Gamma_\varepsilon} = \frac{1}{|B^{n-1}| r^{n-1}} \varepsilon^{n-\gamma(n-1)} + O(\varepsilon^\gamma) \tag{1.4}$$

where $|B^{n-1}|$ denotes the volume of the unit ball of $\mathbb{R}^{n-1}$. Since

- if $\gamma > \gamma_c$, $\lambda(\varepsilon) \to +\infty$ as $\varepsilon \to 0$
- if $1 \leq \gamma < \gamma_c$, $\lambda(\varepsilon) \to 0$ as $\varepsilon \to 0$,

In the case where the particles are completely absorbed at the boundary, the number density of the particles which at time t are at position x and move in the direction ω, $f(t, x, \omega)$ is given by

$$f_\varepsilon(t, x, \omega) = f(0, x - t\omega, \omega) \mathbf{1}_{t \leq \tau_\varepsilon(x,\omega;\gamma)}$$

Thus, a population of point particles undergoing purely absorbing collisions only with the boundary of Z_ε would

- not see the boundary if $\gamma > \gamma_c$
- be instantaneously absorbed by the obstacle in the limit as $\varepsilon \to 0$ if $1 \leq \gamma < \gamma_c$.

More precisely, it can be proven that :

Theorem 1

- Let $n = 2$, and choose $1 \leq \gamma < 2$, $T > 0$, and a compact "observation set" $K \subset \mathbb{R}^2$. Then given any number s with $1 < s < (\gamma - 1)^{-1}$, there exists a constant A such that for any initial data $\phi \in L^\infty(\mathbb{R}^2 \times \mathbf{S}^1)$, the family f_ε of solutions satisfies

$$\left| \int_0^T \int_{K \cap Z_\varepsilon} \int_{\mathbf{S}^1} |f_\varepsilon(t, x, \omega)| d\omega dx dt \right| \leq A \varepsilon^{(1+s-\gamma s)/2} \|\phi\|_{L^\infty}.$$

- Let $n > 2$, and choose $1 \leq \gamma < \frac{n}{n-2/3}$, $T > 0$, and a compact set $K \subset \mathbb{R}^n$. Then given any number s with $1 < s < (\gamma - 1)^{-1}$, there exists a constant A such that for any initial data $\phi \in L^\infty(\mathbb{R}^n \times \mathbf{S}^{n-1})$, the family f_ε of solutions satisfies

$$\left| \int_0^T \int_{K\cap Z_\varepsilon} \int_{\mathbf{S}^{n-1}} |f_\varepsilon(t,x,\omega)| d\omega dx dt \right| \ \leq \ A\varepsilon^{(1+s-\gamma s)/2} \|\phi\|_{L^\infty}.$$

Unfortunately, we do not know of any explicit formula similar to (1.4) for the mean truncated free path, which is a more elaborate quantity related to the problem. However, a weaker form of the previous theorem can be given in terms of the distribution of free paths $\phi_{\varepsilon,\gamma}$, as follows :

Theorem 2

- If $\gamma > \gamma_c = \frac{n}{n-1}$, $\phi_{\varepsilon,\gamma} \to 0$ vaguely as $\varepsilon \to 0$;
- If $n = 2$ and $1 \leq \gamma < \gamma_c = 2$, or if $n > 2$ and $1 \leq \gamma < \frac{n}{n-2/3}$, $\phi_{\varepsilon,\gamma} \to \delta_0$ weakly as $\varepsilon \to 0$.

We recall (see for example [13] pp. 382-383 and Theorem 29.1) that a sequence of measures on $\mathbb{R}^+$ is said to converge vaguely to 0 if the sequence of integrals of any compactly supported continuous function converge to 0; the convergence is weak if the same holds for bounded continuous functions (and not only for the ones having compact support).

As a consequence, the following corollary giving the behavior of the truncated mean free path holds :

Corollary 3

- If $\gamma > \gamma_c = \frac{n}{n-1}$, $l(\varepsilon,T,\gamma) \to T$ as $\varepsilon \to 0$ for all $T > 0$;
- If $n = 2$ and $1 \leq \gamma < \gamma_c = 2$, or if $n > 2$ and $1 \leq \gamma < \frac{n}{n-2/3}$, $l(\varepsilon,T,\gamma) \to 0$ as $\varepsilon \to 0$ for all $T > 0$.

The proof of Theorem 1 and 2 and of Corollary 3 are not recalled here and can be found in [Art1] and [Art3].

1.2 Particles trajectories in a turbulent fluid

Summary. Aluminized propellant may generate alumina deposition behind the submerged nozzle of solid rocket motors. Space shuttle boosters and Ariane 5 launcher experienced such a phenomenon with a respective average of about 900 *kg and* 2 *tons of slag weight. A numerical modelling has thus been developed to predict slag weight. It is based on steady-state, two dimensional, one phase, turbulent flow computations and trajectory calculation of alumina droplets of various diameters. This modelling has been applied with relative success to the Ariane 5 solid rocket motor.*

References : [Proc1], [Proc2], [Conf1].

1.2.1 Objectives

Aluminized propellants are widely used in solid rocket motors to increase specific impulse. Nozzles are also commonly submerged into the motor. Aluminium droplets agglomerate on propellant burning surface. They are steamed into the gas flowfield and burnt for producing alumina (Al_2O_3) droplets. Due to nozzle submergence, a recirculating zone can appear in the aft dome, behind the nozzle. It can trap alumina droplets : a slag deposition process is then triggered. Several solid rocket motors experienced this phenomenon : space shuttle boosters ([15]), Titan IV SRMU boosters or P230 boosters on the Ariane 5 launcher. For instance, the mean slag weight in Titan IV booster is equal to 1985 kg with low dispersion. In RSRM Space Shuttle booster, the mean slag weight is equal to 888 kg, with higher dispersion (the maximum value over the minimum value is equal to 1.8). Our interest in slag formation arose after SSM1 (Sub-Scale Motor 1) test firing. This is a sub-scale motor of a three segment solid rocket motor. A significant amount of alumina was trapped in the aft dome : about 3% of alumina produced during propellant combustion. This slag can have several consequences on performance, on thermal insulation behavior and on thrust vectoring. Slag can also be ejected into the nozzle. The previous analysis of slag formation has been used for a while and applied by several authors. A numerical approach has been developed at Aerospatiale to predict slag weight.It is based on CFD codes for flowfield computation, on a droplet tracking routine and on some assumptions to offset the lack of experimental data, especially concerning droplet size distribution in the combustion chamber. Indeed, the previous description appeared to be too simple. Steaming of droplets along walls and impingements of droplets on the nozzle backface may contribute to slag weight. Another subject of interest concerns turbulent dispersion of droplets.

1.2.2 Numerical model

1.2.2.1 Slag weight prediction

According to Figure 1.2, the way to compute slag weight can be rather straightforward : the droplets which are trapped inside the recirculation zone or which are impinging downstream of the reattachment point are to be numbered. Assuming that only large droplets contribute to slag weight (small ones follow streamlines), the slag weight can be computed from the following equation :

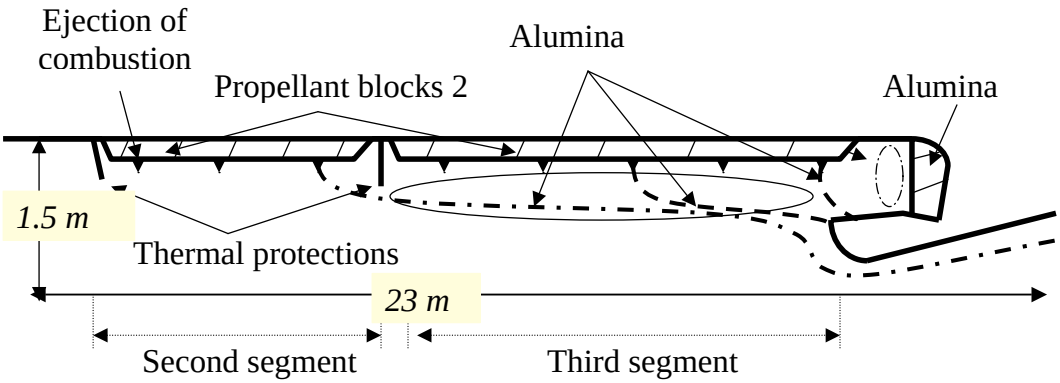

Fig. 1.2 The Ariane 5 booster : schematic description of slag deposition

$$m_{slag} = \int_{t_s}^{t_e} m_{Al_2O_3}(t) Y_{agg}(t) + Y_{trapped}(t) dt$$

The formation of the recirculation zone starts when all propellant behind the submerged nozzle is burnt. Flowfields are computed at several burning times (three or four) and droplets of various sizes are injected along the burning surface. Aluminum combustion is not modelled.

1.2.2.2 Numerical tools

The CFD code used for computing the one phase turbulent flow field is called CEL and has been developed at Aerospatiale (former name of EADS). This Navier Stokes code is an explicit finite volume code, based on unstructured grid (using quadrangles) and Godunov formulation for convective fluxes. A standard $k - \epsilon$ model is used for the turbulence model.

The second component is a droplet tracking routine. The droplets trajectories are computed from the momentum equation which is written in the following form :

$$\frac{d^2 \overrightarrow{X}_d}{dt^2} = \frac{1}{m_d} \overrightarrow{F}_d + \overrightarrow{a} \tag{1.5}$$

In this equation, the drag force (see [14]) is equal to

$$\overrightarrow{F}_d = \frac{1}{8} C_D \rho_g \pi D^2 || \overrightarrow{U}_g - \overrightarrow{U}_d || (\overrightarrow{U}_g - \overrightarrow{U}_d)$$

and the drag coefficient is calculated using the following formula :

$$C_D = \frac{24}{Re_d}(1 + 0.15 Re_d^{0.687})$$

with

$$Re_d = \frac{\rho_g || \overrightarrow{U}_g - \overrightarrow{U}_d ||}{\mu_g}$$

In order to take into account the dispersion of droplets due to the fluid turbulence, a random velocity $\overrightarrow{U}'$ is added to the mean velocity $\overrightarrow{U}_g$. The random velocity is of Gaussian type with a zero mean value and a standard deviation equal to $\sqrt{\frac{2k}{3}}$ where k is the turbulent kinetic energy.

It is applied during a time step $\Delta t = \min(\Delta t_e, \Delta t_l)$ where

$$\Delta t_e = \frac{C_\mu^{\frac{3}{2}} k^{\frac{3}{2}}}{\epsilon ||\overrightarrow{U}'||}$$

and

$$\Delta t_l = \frac{C_\mu^{\frac{3}{2}} k^{\frac{3}{2}}}{\epsilon ||\overrightarrow{U}_g - \overrightarrow{U}_d||}$$

are respectively called the transit time and the Lagrangian time scale.

The momentum equation (1.5) is solved using a predictor-corrector method, which is easy to operate. The only restriction concerns time steps, which are chosen depending on various time scales.

An algorithm has been developed to locate the droplets inside the computational mesh issued from flow field calculation. The resulting tracking routine is two or three dimensional.

1.2.3 Main results

The P230 solid rocket motor of the Ariane 5 launcher, test fired since 1992, has been investigated. It is a three-segmented motor with more than 230 tons of aluminized propellant. A slag weight of more than 2 tons has been trapped. This weight seems to be very consistent throughout several firings. Turbulent flow fields are computed at four burning times. The velocity field and the turbulent energy field k at the combustion time $t = 95s$ are respectively displayed at Figure 1.3 and 1.4.

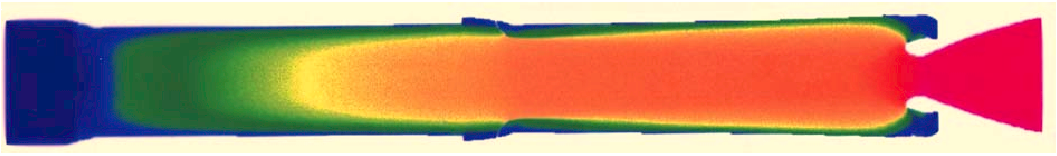

Fig. 1.3 The velocity flow field in the Ariane 5 booster, t=95s

Fig. 1.4 The turbulent energy flow field in the Ariane 5 booster, t=95s

In particular, a high turbulence level is observed inside the third segment of the combustion chamber which is responsible for the turbulent dispersion of droplets and their accumulation inside the submerged nozzle. About this phenomena, some qualitative results are shown on Figure 1.5. The trajectories are significantly dispersed, with droplets impinging the backside of the nozzle, others impinging the case walls and others finding their way towards the nozzle.

For slag weight calculation, a very large number of trajectories is computed for each group of droplets. A group of droplets is defined by : the location of injection at the burning surface X,

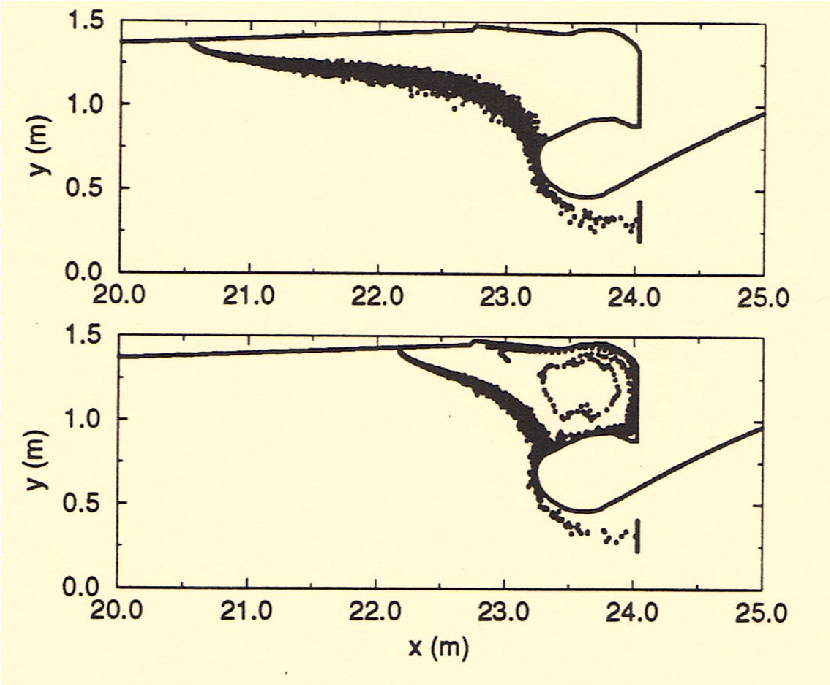

Fig. 1.5 Examples of droplets trajectories

the droplet diameter D and the burning time t. The number of trajectories is typically equal to 500. The data collected for these 500 trajectories are summarized in a function $F(s, t, D, X)$. This function provides the corresponding mass fraction of droplets impinging the motor case walls upstream of abscissa s (see Figure 1.6)

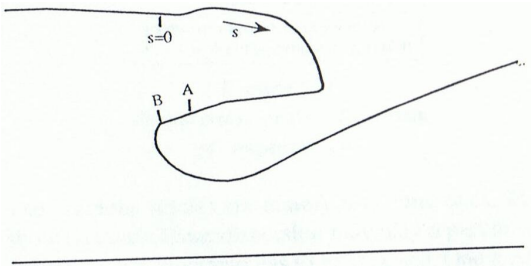

Fig. 1.6 Abscissa along the motor case wall

Two specific locations for the entrapment criterion can be considered : the first one (location called A in Figure 1.6) is the reattachment point and the second one (location B) is a break point in the nozzle backside geometry. Assuming a capture rule ($s < s_A$ or $s < s_B$) and a droplet size distribution, the slag weight can be easily calculated by integration over t, D and X. It is observed that the total amount of slag deposition numerically obtained is very sensitive to the droplet size distribution. Depending on that choice, it ranges from 1500 to 2500 kg and can thus be considered in agreement with the experimental observations. Another observation is the influence of the turbulent dispersion on this value. In case of a deterministic approach, slag weight seems to be always underpredicted.

Chapitre 2
Global optimization methods

Summary. There exists many methods for minimizing a const function J defined from a set $\mathcal{O} \subset \mathbb{R}^n$ to $\mathbb{R}^n$. Among them, the family of evolutionary algorithms, including the well known methods of Genetic Algorithms (GA) and Evolution Strategies (ES) which main principles are recalled in the next subsection, has the major advantage to seek for a global minimum. Unfortunately, this type of method needs to be improved because of the large number of cost function evaluations that are needed. The hybrid optimization methods presented in subsection 2.2 greatly reduce this time by coupling an evolutionary algorithm with a deterministic descent method. Another way to speed up the convergence of an evolutionary algorithm is described in subsection 2.3 and consists in doing fast but approximated evaluations during the optimization process. All these methods are validated in subsection 2.4 on classical analytic test functions.

References : [Cha1], [Art5], [Art6], [Art7], [Art10].

Nota : All the programs presented here are freely available at the following web page :
`http://www.ann.jussieu.fr/~dumas/optimisation-scilab.html`

2.1 Description of classical global optimization methods

2.1.1 Genetic Algorithms (GA)

Genetic Algorithms are global optimization methods directly inspired from the Darwinian theory of evolution of species ([20, 21, 22, 23, 24, 25]). They consist in following the evolution of a certain number N_p of possible solutions, also called population. To each element (or individual) $x_i \in \mathcal{O}$ of the population is affected a fitness value inversely proportional to $J(x_i)$ in case of a minimization problem. The population is regenerated N_g times by using three stochastic principles called selection, crossover and mutation, that mimic the biological law of the 'survival of the fittest'.

The Genetic Algorithms that are used here act in the following way : at each generation, $\frac{N_p}{2}$ couples are selected by using a roulette wheel process with respective parts based on the fitness rank of each individual in the population. To each selected couple, the crossover and mutation principles are then successively applied with a respective probability p_c and p_m. The crossover of two elements consists in creating two new elements by doing a barycentric combination of them with random and independent coefficients in each coordinate. The mutation principle consists

in replacing a member of the population by a new one randomly chosen in its neighborhood. A one-elitism principle is added in order to be sure to keep in the population the best element of the previous generation. Thus, the algorithm writes as :

- *Choice of an initial population* $P_1 = \{x_i^1 \in \mathcal{O}, 1 \leq i \leq N_p\}$
- $n_g = 1$. *Repeat until* $n_g = N_g$
- *Evaluate* $\{J(x_i^{n_g}), 1 \leq i \leq N_p\}$ *and* $m = \min\{J(x_i^{n_g}), 1 \leq i \leq N_p\}$
- 1*-elitism : if* $n_g \geq 2$ *&* $J(X_{n_g-1}) < m$ *then* $x_i^{n_g} = X_{n_g-1}$ *for a random* i
- *for* k *from* 1 *to* $\frac{N_p}{2}$
- *Selection of* $(x_\alpha^{n_g}, x_\beta^{n_g})$ *with a roulette wheel process*
- *with probability* p_c *: replace* $(x_\alpha^{n_g}, x_\beta^{n_g})$ *by* $(y_\alpha^{n_g}, y_\beta^{n_g})$ *by crossover*
- *with probability* p_m *: replace* $(y_\alpha^{n_g}, y_\beta^{n_g})$ *by* $(z_\alpha^{n_g}, z_\beta^{n_g})$ *by mutation*
- *end for*
- $n_g = n_g + 1$.
- *Generate the new population* P_{n_g}.
- *Call* X_{n_g} *the best element.*

2.1.2 Evolution Strategies (ES)

Evolution Strategies (ES) have been first introduced by H.P. Schwefel in the 60's [26, 27, 28]. As it is the case for Genetic Algorithms, it consists in following the evolution of a population of potential solutions through the same three stochastic principles, selection, recombination and mutation. However, contrarily to Genetic Algorithms, the major process is the mutation process and the selection is made deterministic.

The Evolution Strategy that is used here is based on the $(\mu+\lambda)$ selection principle and on the 1/5 rule for the mutation strength. The latter means that the mutation strength σ is readjusted with respect to the rate of successful mutations in a generation : if this rate is greater than 1/5, then σ is multiplied by a factor $\alpha > 1$, else it is divided by the same factor α. An intermediate recombination with two parents is also included. The algorithm thus writes as :

- *Choice of an initial population of* μ *parents :* $P_1 = \{x_i^1 \in \mathcal{O}, \quad 1 \leq i \leq \mu\}$
- $n_g = 1$. *Repeat until* $n_g = N_g$
- *Creation of a population of* $\lambda \geq \mu$ *offsprings* O_{n_g} *by :*
- *Recombination :* $y_i^{n_g} = \frac{1}{2}(x_\alpha^{n_g} + x_\beta^{n_g})$
- *Normal mutation :* $z_i^{n_g} = y_i^{n_g} + \mathcal{N}(0, \sigma)$
- *Update of the mutation strength* σ *with the* 1/5 *rule of parameter* α
- *Evaluate* $\{J(z_i^{n_g}), z_i^{n_g} \in O_{n_g}\}$
- $n_g = n_g + 1$
- *Selection of the best* μ *new parents in the population* $P_{n_g} \cup O_{n_g}$.
- *Call* X_{n_g} *the best element.*

2.2 Adaptive hydrid optimization method (AHM)

All the previous methods that make evolve a population of potential solutions are very time consuming because of the large number of evaluations of the functional that are needed. The idea of coupling them with a gradient-based method for a more efficient local search, leading to what is called hybrid methods, has shown its efficiency in many situations in the last decade ([29, 30,

31, 32, 33]), for instance for aerodynamic shape optimization. Unfortunately, the introduction of new parameters in hybrid methods reduce their range of application and make them 'problem-dependent'.

The present method, called Adaptive Hybrid Method (AHM) try to remedy to these drawbacks by answering on a fully adaptive way to the three fundamental questions in the construction of a hybrid method :

- Question 1 : when do we shift from the global search to the local search ?
- Question 2 : when do we come back to the global search ?
- Question 3 : on which elements do we apply a local search ?

In order to answer to Questions 1 and 2, the AHM method uses some criteria introduced in the pioneer work of [32] whereas a new strategy called 'reduced clustering' allows to answer to Question 3 on a fully adaptive way.

2.2.1 The shift from global to local (the answer to Question 1)

The shift from a global search to a local search is useful when the exploration ability of the global search is no longer efficient. To this aim, a statistical coefficient associated to the cost function repartition values is introduced. It is equal to the ratio of the mean evaluation of the current population X to its corresponding standard deviation :

$$CV = \frac{m}{\sigma} = \frac{\text{mean}\{J(x),\, x \in X\}}{\sqrt{\text{Var}\{J(x),\, x \in X\}}}$$

and is named coefficient of variation. A local search will be called when this ratio is increasing between two consecutive genrations of the global search.

2.2.2 The shift from local to global (the answer to Question 2)

The local search, a gradient based method with a line search strategy, is aimed at making locally decrease the cost function more efficiently than the normal random mutation. However, this gain must be counterbalanced each time before evaluating a new gradient vector with a characteristic gain of the global method. More precisely, the local search will here continue while :

$$G_{local} > G_{global}$$

where G_{local} is equal to the gain when passing from a point to the next one in the steepest descent algorithm and G_{global} is the gain of the last global phase (evaluated with the decrease of m, the mean evaluation of the current population). Both gains are scaled with the number of evaluations of the cost function needed to achieve them.

2.2.3 The reduced clustering strategy (the answer to Question 3)

In order to spread as much as possible the local search in the whole domain, the population is divided into a certain number of sub-populations, called clusters. To do so, a very classical and fast algorithm is used where each cluster is constructed such that all its associated elements

are closer to its center of mass than to any other. After this preliminary step called clustering, the local search is applied to the best element (with respect to J) of each cluster.

A careful study of the appropriate number of clusters has never been done even though it appears to be rather important for the algorithm performance. To overcome the difficulty of choosing this number,a method called reduced clustering is proposed. In this method, the number of clusters is progressively decreased during the optimization process. It corresponds to the natural idea that the whole process will progressively focus on a reduced number of local minima. To do so, a deterministic rule of arithmetic decrease plus an adaptive strategy including the aggregation of too near clusters has been used here. Note that the effect of the initial number of clusters has also been investigated on test functions. It appears that a initial number of clusters between 5% and 20% of the population will give the best results. Below 5%, some premature convergence can be observed whereas above 20%, the convergence speed may be reduced. The value of 10% will thus be adopted for all the simulations presented below.

2.3 Genetic Algorithms with approximate evaluations (AGA)

Another idea to speed up the convergence of an evolutionary algorithm when the computational time of the cost function $x \mapsto J(x)$ is high, is to take benefit of the large and growing data base of exact evaluations by making fast and approximated evaluations $x \mapsto \tilde{J}(x)$ leading to what is called surrogate or meta-models (see [34, 35, 36, 37, 38, 39, 40]). In the present work, the chosen strategy consists to perform exact evaluations only for all the best fitted elements of the population (in the sense of $\tilde{J}$). The new algorithm, called AGA is thus deduced from the Genetic Algorithm described in section 2.1.1 by changing the evaluation phase into the following :

- *Make approximated evaluations* $\{\tilde{J}(x_i^{n_g}), 1 \leq i \leq N_p\}$
- *For the best* $N_b(n_g)$ *elements in terms of* $\tilde{J}$*, make exact evaluations of them.*

The shape of the function $n_g \rightarrow \frac{N_b(n_g)}{N_p}$ representing the rate of exact evaluations at generation n_g is the first choice to make. In any case, it has to be equal to 1 for the first $N_{geninit}$ generations. Then, two choices have been tested :

- In the first version of the AGA algorithm (presented in [Art6], and [Art7]), the exact evaluations are made only for the elements which have a lower value with $\tilde{J}$ than the best value previously obtained with J, and for a randomly chosen element.
- In the second version of the AGA algorithm (used in [Art12]), the number of exact evaluations is fixed and is linearly decreasing from a value $r \in]0, 1[$ to 0.

The interpolation method chosen here comes from the field of neural networks and is called RBF (Radial Basis Function) interpolation ([34]). Suppose that the function J is known on N points $\{T_i, 1 \leq i \leq N\}$, the idea is to approximate J at a new point x by making a linear combination of radial functions of the type :

$$\tilde{J}(x) = \sum_{i=1}^{n_c} \psi_i \Phi(||x - \hat{T}_i||) \tag{2.1}$$

where :

- $\{\hat{T}_i, 1 \leq i \leq n_c\} \subset \{T_i, 1 \leq i \leq N\}$ is the set of the $n_c \leq N$ nearest points to x for the euclidian norm $||.||$, on which an exact evaluation of J is known.
- Φ is a radial basis function chosen in the following set :

$$\Phi_1(u) = \exp(-\frac{u^2}{r^2})$$

$$\Phi_2(u) = \sqrt{u^2 + r^2}$$
$$\Phi_3(u) = \frac{1}{\sqrt{u^2 + r^2}}$$
$$\Phi_4(u) = \exp(-\frac{u}{r})$$

for which the parameter $r > 0$ is called the attenuation parameter.

The scalar coefficients $(\psi_i)_{1 \leq i \leq n_c}$ are obtained by solving the least square problem of size $N \times n_c$:

$$\text{minimize} \quad err(x) = \sum_{i=1}^{N} (J(T_i) - \tilde{J}(T_i))^2 + \lambda \sum_{j=1}^{n_c} \psi_j^2$$

where $\lambda > 0$ is called the regularization parameter.

In order to attenuate or even remove the dependance of this model to its attached parameters, a secondary global optimization procedure (namely a classical GA) has been over-added in order to determine for each x, the best values (with respect to $err(x)$) of the parameters n_c, $r \in [0.01, 10]$, $\lambda \in [0, 10]$ and $\Phi \in \{\Phi_1, \Phi_2, \Phi_3, \Phi_4\}$. As this new step introduces a second level of global optimization, it is only reserved to cases where the time evaluation of $x \mapsto J(x)$ is many orders of magnitude higher than the time evaluation of $x \mapsto \tilde{J}(x)$.

Note that in the the second version of AGA used in [Art12], this procedure is simpler : n_c, Φ and r are fixed and the least square problem is changed into a $n_c \times n_c$ linear system to solve.

2.4 Results on test functions

Both the Adaptive Hybrid Method (AHM) and the Approximated Genetic Algorithm (AGA) have been tested on various analytical test functions, and among them the well known Rastrigin function of parameter a :

$$Rast_a(x_1, ..., x_n) = \sum_{i=1}^{n} \left(x_i^2 - a\cos(2\pi x_i)\right) + an$$

defined on $\mathcal{O} = [-5, 5]^n$ for which there exists many local minima and only a global minimum located at $x^* = (0, ..., 0)$. Note that the number of local minima in $\mathcal{O}$ is always equal to 11^n but the attraction basins become steeper when $a > 0$ takes a higher value.

A statistical comparison based on 40 independent runs for each method, has been made between a classical population based method, either a GA or an ES, and the associated AHM method or the AGA method (in its second version).

The result are displayed on Figure 2.1 to 2.4. For each method, the average best obtained value is plotted with respect to the number of function evaluations needed to achieve it.

In the case of the AHM method, any gradient evaluation counts for n evaluations of the cost function as it is the case in many real applications for which the gradient has to be approximated by finite differences.

In the case of the AGA method, only the exact evaluations of the cost function are taken into account.

2.4.1 Results obtained for the AHM method

For the simulations presented below, the population size for the GA is either equal to $N_p = 40$ if $n = 6$ or $N_p = 100$ if $n = 20$ whereas $(\lambda, \mu) = (35, 5)$ for the ES. A maximal number of function evaluation is allowed, either equal to 4000 when $n = 6$ and 10000 when $n = 20$.

2.4.1.1 Result for the $Rast_1$ function

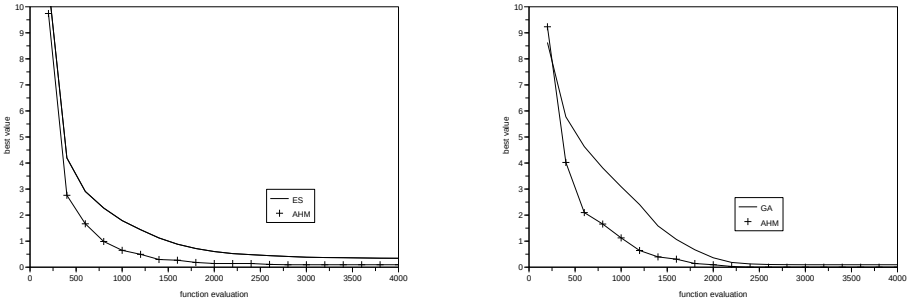

Fig. 2.1 Comparison of ES (left) and GA (right) with AHM on $Rast_1$, $n = 6$

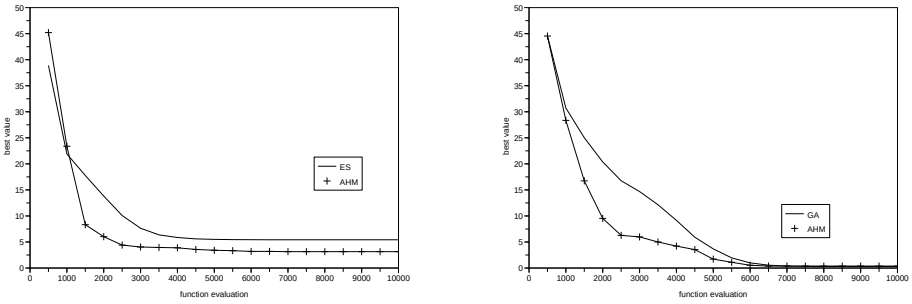

Fig. 2.2 Comparison of ES (left) and GA (right) with AHM on $Rast_1$, $n = 20$

A comparison between the use of a GA or an ES as the global search method for the AHM method is made on the $Rast_1$ function with 6 and 20 parameters. The results, respectively displayed on Figures 2.1 and 2.2, show that the AHM method takes advantage compared to a pure ES or a pure GA in terms of the convergence speed to the optimal best value. In this situation, the GA results are better than the ES results. In particular, there are no longer cases of premature convergence to a local minima, particularly if $n = 20$. It implies that, in this case, the AHM method with a GA base performs better than the AHM with an ES base. However, it is necessary to be careful about any generalization of this observation.

2.4.1.2 Result for the $Rast_{10}$ function

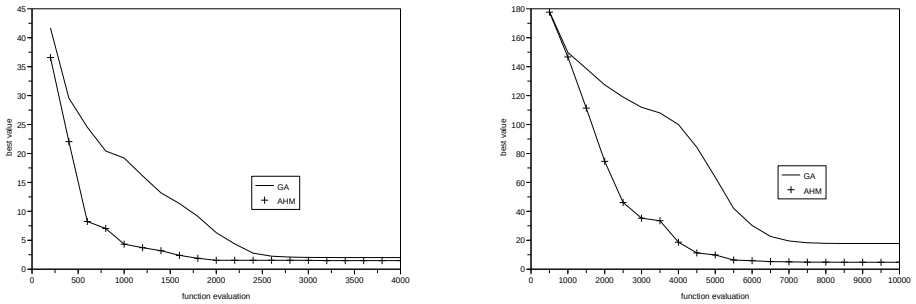

Fig. 2.3 Comparison of GA with AHM on $Rast_{10}$, $n = 6$ (left) and $n = 20$ (right)

Another example of comparison between a pure GA and the corresponding AHM for the $Rast_{10}$ function is visible on Figure 2.3. A statistical comparison is also drawn on Table 2.1 where the mean, the best, and the worst value for GA and AHM are displayed after 5000 evaluations of the $Rast_{10}$ function with $n = 20$.

Method	Mean obtained value	Best value	Worst value
GA	63.56	45.54	90.49
AHM	9.82	4.97	14.06

Tableau 2.1 Comparison of GA and AHM after 5000 evaluations of $Rast_{10}$, $n = 20$

The conclusions are the same than for the $Rast_1$ function but with larger differences between both methods, always in the advantage of AHM. In other words, it means that the interest of using AHM increases with the difficulty of the problem (related here to the steepness of local minima attraction basins).

2.4.2 Results obtained for the AGA method

The results obtained by the AGA method and the associated GA are compared in the case of the $Rast_1$ function, with 6 and 20 parameters respectively (see Figure 2.4). The population size for the GA is either equal to $N_p = 40$ if $n = 6$ or $N_p = 160$ if $n = 20$. A maximal number of functions evaluations is allowed, either equal to 2500 when $n = 6$ and 12000 when $n = 20$.

In both simulations, the specific parameters associated to the AGA method are respectively equal to $N_{geninit} = 2$ (number of initial generations with only exact evaluations) and $n_c = 16$ (size of the sampling to compute the approximated function).

As in the case of the AHM method, the AGA overperforms the GA method in terms of exact evaluations of the cost function to achieve a given level of convergence. A reduction rate approximately equal to 3 is observed here in the case of the Rastrigin function.

Compared to other results found in the literature for the Rastrigin function (see for instance [33, 28]), the results obtained either with the AHM or the AGA method are very competitive. Moreover, it is worth noticing that the same general conclusions have been observed for other

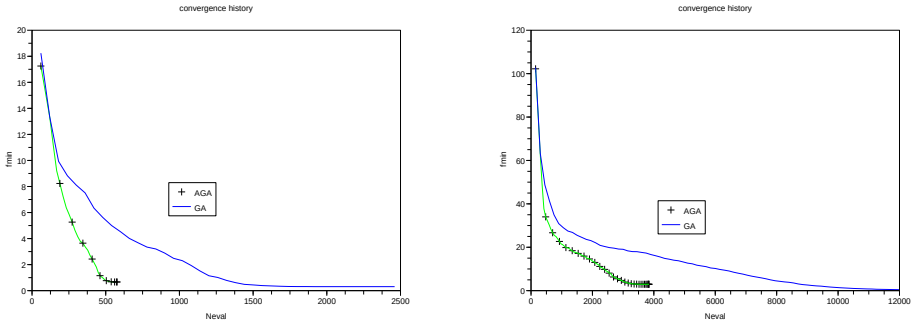

Fig. 2.4 Comparison of GA with AGA on $Rast_1$, $n = 6$ (left) and $n = 20$ (right)

test functions similar to the Rastrigin function, that is with many local minima, namely the Ackley and the Griewank functions.

Thus, the use of AHM or AGA will have two positive effects compared to a pure global search strategy (GA, ES, etc...) : at the early stage of the computation, it will enhance the decrease of the cost function and, at the late stage, it may also improve the final optimal solution. Such effects are particularly interesting in an industrial process where the computational time can be very large and also where any small improvement to the optimal solution can lead to significant productivity gains, as it will be seen in the next chapter.

Chapitre 3
Global optimization with ODE or PDE constraints : applicative examples

This chapter presents various global optimization problems that have been solved with the methods presented above. Each section of this chapter is directly linked to an industrial or a medical application and can be formulated as a global optimization problem with ODE or PDE constraints.

3.1 Optimization with ODE constraints for telecommunications

Summary. High channel count filters based on non-chirped apodized Sampled Fiber Bragg Gratings (SFBG) have been synthesized using evolutionary algorithms, leading to better resuts than the classical Sinc-type apodization method. Moreover, the grating solutions produced by this approach are easier to build from an industrial point of view.

References : [Art8], [Art9].

3.1.1 Objectives

The use of new optical fiber devices in the telecommunication sector has known an important development in the last few years. Among them, Sampled Fiber Bragg Gratings (SFBG) based devices represent an attractive alternative for applications such as multichannel filtering and multiwavelength laser sources [41]. The main SFBG functionality is to ensure the choice of desired wavelengths.

We focus here on the design of SFBG multichannels filters that exhibit periodic maxima, called channels or peaks, in their spectrum. There is an important demand for optimization methods for the associated inverse problem that consist to design a SFBG with a desired reflection spectrum [44]. These methods need to perform global optimization as it is observed that the associated cost function hs multiple minima [43].

3.1.2 Modelization of Fiber Bragg Gratings

3.1.2.1 The coupled mode model

A Fiber Bragg Grating (FBG) is an optical fiber with a perturbed refractive index. Its functionality is, starting from a wavelength band E, to reflect a part of the wavelength band $E-$, called reflection spectrum, and to let the complementary band $E+$, called transmitted spectrum pass (see figure 3.1).

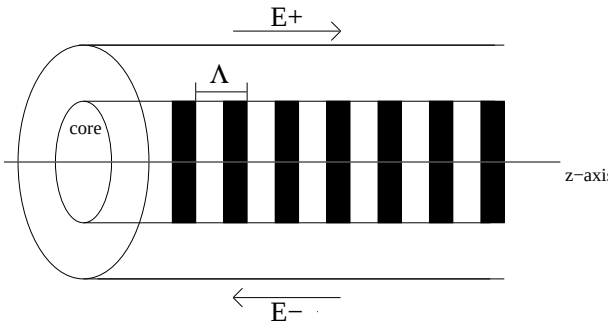

Fig. 3.1 Fiber Bragg grating diagram

FBG are made exposing a classical optical fiber to a Laser Ultra-Violet radiation [41]. This radiation modify the refractive index of the optical guide core. Thus, the FBG refractive index n varying as along the fiber axis z is given by :

$$n(z) = n_0 + \delta n(z)$$

where n_0 is the initial refractive index and δn the UV exposure refractive index perturbation which is of the form :

$$\delta n(z) = \overline{\delta n}(z)\cos(\frac{2\pi}{\Lambda}z) \quad z \in [0, L]$$

In this expression, L is the fiber length, Λ is the grating period and $\overline{\delta n}(z)$ is called apodization.

In order to extract a mathematical model which permit to compute the reflection spectrum of a given FBG, we assume that for any wavelength λ in the transmission band E there exist only two counter propagating guided modes in the FBG, the reflected and transmitted modes of respective amplitude $b_T(z, \lambda)$ and $b_R(z, \lambda)$. These two functions are solution of the following system of coupled ordinary differential equations :

$$\frac{db_T(z,\lambda)}{dz} - i\beta b_T(z,\lambda) = \overline{q}(z)b_R(z,\lambda) \tag{3.1}$$

$$\frac{db_R(z,\lambda)}{dz} + i\beta b_R(z,\lambda) = q(z)b_T(z,\lambda) \tag{3.2}$$

for every $z \in [0, L]$ and every wavelength $\lambda \in B$ and with the boundary conditions

$$b_T(0, \lambda) = 1 \quad \text{and} \quad b_R(L, \lambda) = 0$$

In these equations, β is a parameter homogeneous to a frequency and is linked to λ by the relation :

$$\beta = 2\pi n_0(\frac{1}{\lambda} - \frac{1}{2n_0\Lambda})$$

whereas q is called the coupling function and is defined as :

$$q(z) = -\frac{i\pi}{2\Lambda n_0}\overline{\delta n}(z)$$

.

The reflection spectrum of the FBG corresponds to the function $\lambda \mapsto \rho(\lambda)$ where

$$\rho(\lambda) = |b_R(0,\lambda)|^2$$

In order to approximate the reflection spectrum, we use the transfer matrix method [41]. Its principle consists first to compute the exact solution of (3.1)-(3.2) when the coupling coefficient q is constant ($q = q_0$). In this case,

$$\rho(\lambda) = \frac{-q_0 \operatorname{sh}(\gamma L)}{\gamma \operatorname{ch}(\gamma L) - i\beta \operatorname{sh}(\gamma L)}$$

where $\gamma^2 = |q_0|^2 - \beta^2$.

The considered FBG is then decomposed into a set of N elementary fibers of length $\Delta = \dfrac{L}{N-1}$ with a constant refractive index. For the j^{th} uniform section, we have :

$$\begin{pmatrix} b_T((j+1)\Delta,\lambda) \\ b_R((j+1)\Delta,\lambda) \end{pmatrix} = T_j \begin{pmatrix} b_T(j\Delta,\lambda) \\ b_R(j\Delta,\lambda) \end{pmatrix}$$

where T_j is a transfer matrix given by :

$$T_j = \begin{pmatrix} \operatorname{ch}(\gamma\Delta) + i\frac{\beta}{\gamma}\operatorname{sh}(\gamma\Delta) & \frac{\bar{q}_j}{\gamma}\operatorname{sh}(\gamma\Delta) \\ \frac{q_j}{\gamma}\operatorname{sh}(\gamma\Delta) & \operatorname{ch}(\gamma\Delta) - i\frac{\beta}{\gamma}\operatorname{sh}(\gamma\Delta) \end{pmatrix}$$

with $q_j = q(j\Delta)$. Using the following notation : $T = T_{N-2}\dots T_0 \equiv [T_{i,j}]_{(i,j)}$, we have the approximation of reflection spectrum :

$$\tilde{\rho}(\lambda) = -\frac{T_{2,1}}{T_{2,2}}$$

The cost of this method is $O(NM)$ times the cost of the evaluation of the matrix T_j with M being the number of points of the spectral discretization.

As we can see, for the considered FBG modelling, the reflection spectrum can be computed knowing only the apodization $\overline{\delta n}$ of the fiber.

3.1.2.2 Sampled FBG

A Sampled FBG (SFBG) is a fiber made with a FBG pattern reproduced R times. This is an efficient and simple technique to construct an optical filter that exhibits periodic maxima in its reflection spectrum. Using the coupled mode theory [41], it can be shown that a SFBG structure leads to a spectrum which is a comb distribution of peaks with identical response and with a wavelength separation $\Delta\lambda = \dfrac{2Rn_0\Lambda^2}{L}$.

The computation of the reflection spectrum of a SFBG remains unchanged compared to what is exposed in the previous paragraph, though more time consuming.

3.1.3 Main results

A global optimization method based on Genetic Algorithms has been successfully applied to solve various examples of inverse problems relative to the design of SFBG. In the case presented here, the objective is to construct a multichannel filter with the following characteristics : the spectra is centered around $1552.5nm$ and consist of $N_{peaks} = 16$ totally reflective identical channels spaced of $\Delta\lambda = 0.8nm$. The unperturbed refractive index and the total length of the SFBG are respectively fixed equal to $n_{eff} = 1.45$ and $L = 103.9mm$.

3.1.3.1 Current design of multichannel filters based on SFBGs

The method usually used in industry was initiated by Ibsen et al. [42]. They have shown the possibility to inscribe inside the fiber core a Sinc-shaped apodization profile with a continuous writing technique :

$$\overline{\delta n}(z) = \delta n_{max} \frac{\sin(\frac{2N_{peaks}\pi z}{P})}{\frac{2N_{peaks}\pi z}{P}} \quad z \in [-\frac{P}{2}, \frac{P}{2}]$$

Where δn_{max} is the maximum apodization variation.

These technique allow to generate filters which exhibit a comb distribution of N_{peaks} channels in their spectra. But this type of apodization profile suffers several drawbacks :

- The Sinc function consists of a main lobe and secondary side loops which proportion must be perfectly respected. This profile is not homogeneously distributed along the pattern. So it may give rise to a non linear regime during the UV-writing.
- The δn_{max} value has to be high. High values are difficult to reach in practice and they imply to use very photosensitive fibers.
- The number of secondary side loops of the Sinc function is directly proportional to the total number N_{peaks} channels. To physically express the sign change of the Sinc function, discrete phase shifts must be inserted between each side loop. So a great number of phase shifts are required as the number of channels increases.

For all these reasons a perfect and expensive control and mastering of the writing process is required to apply this method.

3.1.3.2 Numerical modelling

In order to find a SFBG with the desired spectral response and associated with an index modulation with some 'interesting' industrial characteristics in comparison to the Sinc-profile : smooth enough, slowly varying and reduced sign change number and symmetric, apodization profiles are generated by spline interpolation through a reduced number of N_S points equally distributed along the first half of the sampling pattern and completed by parity. We will thus choose a value of N_S high enough to ensure a large number of peaks in the spectral response but small enough to ensure improvement in the apodization profile. More precisely, the corresponding search space of the optimization problem is a hypercube :

$$\Omega_{N_S} = [-\overline{n}_{max}, \overline{n}_{max}]^{N_S}$$

where $\overline{n}_{max}$ the maximum amplitude variation is a design constraint. Here $\overline{n}_{max} = 5 \times 10^{-4}$ and $N_S = 9$ respectively for the inverse problem presented here.

The functional on Ω_{N_S} to minimize is an error-type function, as in any inverse problem, defined by :

$$J_{N_c}(x) = \sum_{i=1}^{N_c} (\rho(x)(\lambda_i) - \rho_{target}(x)(\lambda_i))^2$$

In the above expression, the reflection spectrum function $\rho(x)$ associated to a SFBG with an apodization $x \in \Omega_{N_s}$ is a function defined from the transmission band $[\lambda_{min}, \lambda_{max}]$ to $[0, 1]$. On the other hand, $\rho_{target}(x)$ denotes the nearest reflection spectrum function to $\rho(x)$ matching the desired requirements, namely N_{peaks} transmitted wavelengths with a perfect transmission rate and separated by $\Delta\lambda$:

$$\rho_{target}(x)(\lambda) = \begin{cases} 1 \ if \ \lambda \in \{\lambda_x, \lambda_x + \Delta\lambda, \ldots, \lambda_x + (N_{peaks} - 1)\triangle\lambda\} \\ 0 \text{ elsewhere} \end{cases}$$

From an industrial point of view, note that an exploitable peak should only have a reflectivity superior to 0.95. Both functions $\rho(x)$ and $\rho_{target}(x)$ are evaluated here on $M = 1200$ wavelengths equally distributed on the transmission band.

3.1.3.3 Results and discussion

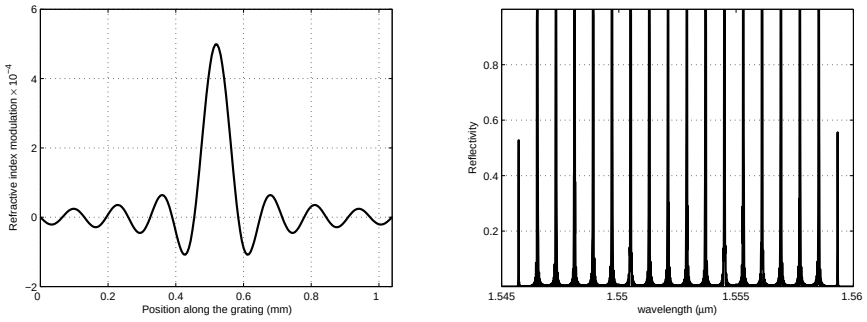

Fig. 3.2 16 peaks multichannel filter with Sinc filter. Left : Apodization profile, right : Associated spectrum.

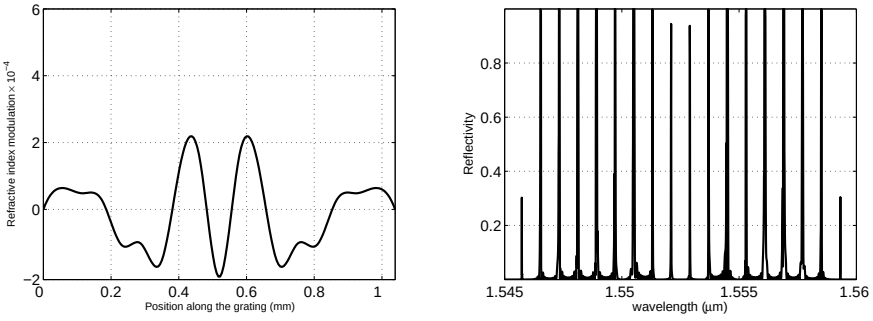

Fig. 3.3 16 peaks multichannel filter with GA filter. Left : Apodization profile, right : Associated spectrum.

Figure 3.2 and 3.3 show the apodization profile and the associated reflection spectrum of two different filters, respectively Sinc and GA (i.e. obtained by these procedures). The Sinc filter has a cost function equal to 6.59 whereas the GA filter gives 5.83. These two values of the cost function show that GA algorithm has led to better solutions in terms of reflection characteristics than the Sinc profile. This is visible in the second column of Figure 3.3 on the undesirable side peaks amplitude which are reduced to 0.3 in the GA one to be compared to the value of 0.4 for the Sinc profile.

In addition, optimized profiles are more suitable for industrial realization as the number of necessary phase shifts (when $\overline{\delta n}(z) = 0$) is only 6 for the GA profile against 14 for the Sinc-profile and the index modulation of profiles is more homogeneously distributed along the pattern and does not exhibit any dominant lobe. A last improvement concerns the maximum amplitude of the apodization profile which has been reduced to $\Delta\overline{n}_{max} = 2. \times 10^{-4}$ for the GA profile compared to $5. \times 10^{-4}$ for the Sinc filter.

3.2 Optimization with PDE constraints in a 1D space for medicine

Summary. The inverse problem corresponding to the identification of the main parameters of a 1D model for blood flow has been successfully solved. It has shown in particular that the optimal parameters may be different from those expected from a formal averaging. Moreover, in the case of an artery with a loss of compliance in some portion, the knowledge of only one area section profile downstream is enough to locate the exact position of this disease portion.

References : [Art11], [Proc6]

3.2.1 Objectives

In order to reduce the cost of complex 3D fluid-structure computations of blood flow in arteries, a one dimensional model has been developed based on the averaging of the general three dimensional equations [46, 48]. Under a certain number of hypotheses for the artery flow and geometry, it computes the section area $A(t,z)$ and the volumic flux $Q(t,z)$ at any longitudinal position z and time t. Such model is interesting for three main reasons : first, it drastically reduces the computational time of the 3D model, secondly, its two unknowns are quantities that can be experimentally obtained by non invasive techniques and finally, it allows to recover all the other hemodynamic variables like blood pressure that are more difficult to measure.

The general objective of this work is to show that the parameters of this 1D model can be fitted either with the results of 3D computations or with experimental values measured at a finite number of positions z and times t. In particular, it includes the case of an artery with a large compliance step which occurs when this artery is partially obturated by atherosclerotic plaques (see Figure 3.4). In this case, it can be important to locate precisely the position of the plaque before putting a permanent metallic implant used to prop open arteries and called stent [47]. Even after this operation, note that the artery will still experience a compliance step at the stent location.

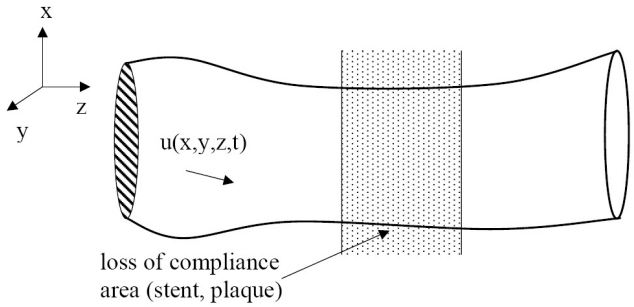

Fig. 3.4 Blood flow in an artery : the 3D model

The main parameter of the 1D model that has to be fixed by solving an inverse problem is a function of z, called β, directly linked to the compliance value of the artery. The problem of the amount of information needed to recover the correct shape of β is in particular discussed.

3.2.2 The 1D model of blood flow

3.2.2.1 From 3D to 1D

The blood velocity and pressure in an artery satisfy the following Navier Stokes equations in a 3D domain similar to the one depicted in Figure 3.4 :

$$\begin{cases} \dfrac{\partial u}{\partial t} + (u \cdot \nabla)u + \dfrac{1}{\rho}\nabla p + \operatorname{div}\left(\nu \dfrac{\nabla u + (\nabla u)^T}{2}\right) = 0 \\ \operatorname{div}(u) = 0 \end{cases}$$

where ρ and ν respectively denote the density and the kinematic viscosity of the blood. Because of the compliance of the arterial wall, theses equations must be coupled with an appropriate model of the vessel wall dynamics. Moreover, this compliance can vary along the artery, for instance because of the formation of atherosclerotic plaques or the presence of a stent (see Figure 3.4).

In order to reduce the computational time needed to solve these equations, a 1D model has been proposed by assuming that the artery has a cylindrical geometry with a circular cross section (see Figure 3.5).

After averaging the 3D Navier Stokes equations over each cross section, a system with two unknowns, $A(t,z)$ the section area at time t and position $z \in [0, L]$, and $Q(t,z)$ the volumic flux, is derived (see [46] for more details) :

$$\begin{cases} \dfrac{\partial A}{\partial t} + \dfrac{\partial Q}{\partial z} = 0 \\ \dfrac{\partial Q}{\partial t} + \dfrac{\partial}{\partial z}\left(\dfrac{Q^2}{A}\right) + \dfrac{A}{\rho}\dfrac{\partial p}{\partial z} + K_r \dfrac{Q}{A} = 0 \end{cases} \tag{3.3}$$

In this system, p denotes the average pressure and is determined by the following law :

$$p(t,z) = \beta(\sqrt{A} - \sqrt{A_0}) \tag{3.4}$$

where A_0 represents the section area of the artery at rest.

The coefficients K_r and β appearing in the model are respectively linked to the blood viscosity and the elastic properties of the artery. In view of the possible applications, β will thus take the form of a function of z. A formal derivation from the $3D$ to the $1D$ model lead to the following expression for the parameter β :

$$\beta(z) = \frac{4\sqrt{\pi}h_0 E(z)}{3A_0}$$

where h_0 and $E(z)$ respectively denote the thickness and the Young modulus of the vessel wall.

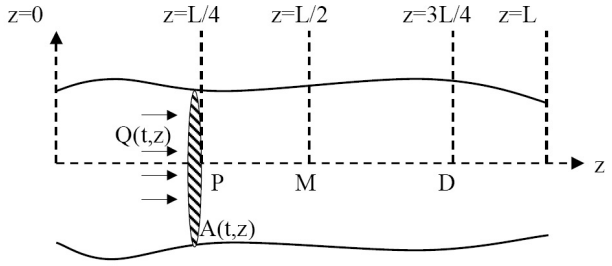

Fig. 3.5 Blood flow in an artery : the 1D model

The 1D model 3.3-3.4 can be rewritten in a conservative form :

$$\frac{\partial U}{\partial t} + \frac{\partial F(U)}{\partial z} = B(U) \tag{3.5}$$

where $U = \begin{pmatrix} A \\ Q \end{pmatrix}$ and

$$F(U) = \begin{pmatrix} Q \\ \frac{Q^2}{A} + \frac{\beta}{3\rho} A^{\frac{3}{2}} \end{pmatrix}, \quad B(U) = \begin{pmatrix} 0 \\ -K_r \frac{Q}{A} + \frac{A}{\rho} \frac{d\beta}{dz} (\sqrt{A_0} - \frac{2}{3}\sqrt{A}) \end{pmatrix}$$

It can be observed that this system is hyperbolic, as the Jacobian

$$H = \frac{\partial F}{\partial U} = \begin{pmatrix} 0 & 1 \\ \frac{\beta\sqrt{A}}{2\rho} - (\frac{Q}{A})^2 & 2\frac{Q}{A} \end{pmatrix}$$

has always two real and distinct eigenvalues for all the allowable values of U. The PDE system is then completed by two appropriate boundary conditions, one at each end. A pressure profile is in particular imposed at the entrance.

3.2.2.2 Numerical discretization

The equations of the 1D model are discretized in their conservative form (3.5) by using a second order Taylor Galerkin scheme. Denote Δt the chosen time step, then the vector of unknowns U^n at time $t_n = n\Delta t$ satisfies the following time-marching scheme :

$$U^{n+1} = U^n - \Delta t \frac{\partial}{\partial z}(F^n + \frac{\Delta t}{2} \frac{\partial F}{\partial U}^n B^n) - \frac{\Delta t^2}{2}(\frac{\partial B}{\partial U}^n \frac{\partial F^n}{\partial z} - \frac{\partial}{\partial z}(\frac{\partial F}{\partial U}^n \frac{\partial F^n}{\partial z})) + \Delta t(B^n + \frac{\Delta t}{2} \frac{\partial B}{\partial U}^n B^n)$$

The spatial discretization is then done by using linear finite elements on the subdivision $(z_i)_{i\in\{0,\dots,N\}}$ of $[0, L]$.

3.2.2.3 Numerical tests

Two numerical tests have been performed in order to see the influence of a compliance loss on the transmission of a pressure impulse. In both cases, the same pulsatile pressure, displayed on Figure 3.6, is imposed at the entrance of an artery of length $L = 4$cm.

For both cases, the section area at rest A_0 is chosen constant and equal to 0.780362 cm^2 whereas $K_r = 0.75$. On the contrary, the coefficient β is different between the two test cases (see below).

The initial conditions for A and Q are chosen constant in space, respectively $A(0, z) = A_0$ and $Q(0, z) = 0$.

Test cas 1 : artery with a constant compliance
In this first test case, the compliance is chosen constant and taken equal to its formal expression (4) with $E_0 = 4.10^6$ dynes/cm^2 and $h_0 = 0.1$ cm, that is :

$$\beta_{formal} = 1211372\,\text{dynes}/cm^3$$

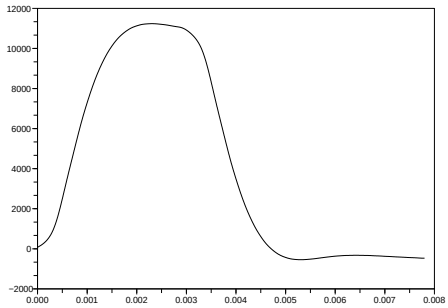

Fig. 3.6 Blood pressure at entrance (in dynes/cm^2)

A uniform spatial discretization of $[0, L]$ is chosen with $N = 128$ and the time step is taken equal to 10^{-5}.

The results are depicted on Figure 3.7. The two unknowns A and Q, as well as the pressure issued from them by the relation 3.4, are displayed at three different points inside the artery, respectively located at $z = \frac{L}{4}$, $\frac{L}{2}$ and $\frac{3L}{4}$ and called points P, M and D (see Figure 3.5).

In this case, it can be observed that the pressure impulse travels along the artery at a constant speed and with minor changes during its propagation.

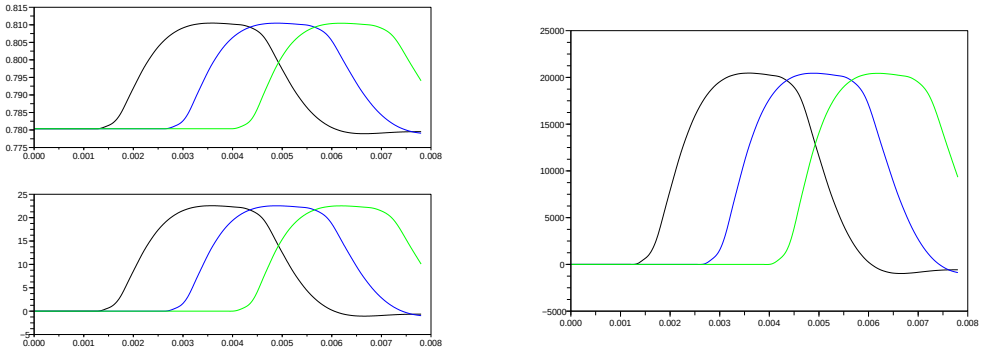

Fig. 3.7 Section area A (top left), volumic flux Q (bottom left) and pressure (right) at points P, M and D for the constant compliance case.

Test case 2 : artery with a variable compliance

The second test case studies the propagation of the same impulse pressure in a case where the compliance of the artery is supposed to be variable with z.

More precisely, the value of β is taken 10 times higher in a portion located between $a_1 = 1.5$ cm and $a_2 = 2.5$ cm. Such abrupt change can be linked for instance by the presence of a stent or of atherosclerotic plaques at this location inducing a severe loss of compliance. Numerically, the function $\beta \to \beta(z)$ has to be at least C^2 because of the presence of the term $\dfrac{d\beta}{dz}$ in $B(U)$. A smoothing procedure with a small transition parameter δ is thus done leading to the shape depicted in Figure 3.8 with

$$(\beta_1, \beta 2) = (\beta_{formal}, 10\beta_{formal}) \quad \text{and} \quad (a_1, a_2) = (1.5, 2.5)$$

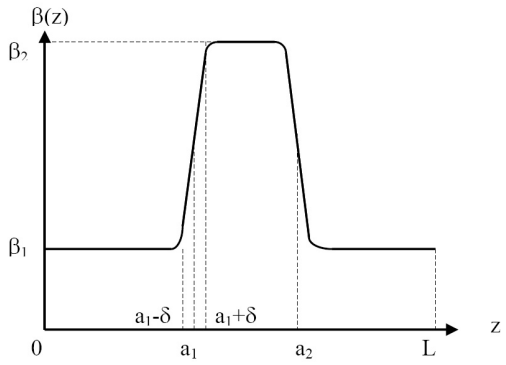

Fig. 3.8 Function $z \to \beta(z)$, variable compliance case

Because of the large value of $\dfrac{d\beta}{dz}$ near the points $z = a_1$ and $z = a_2$, the spatial mesh has to be refined locally and the time step is now equal to 3.10^{-6}.

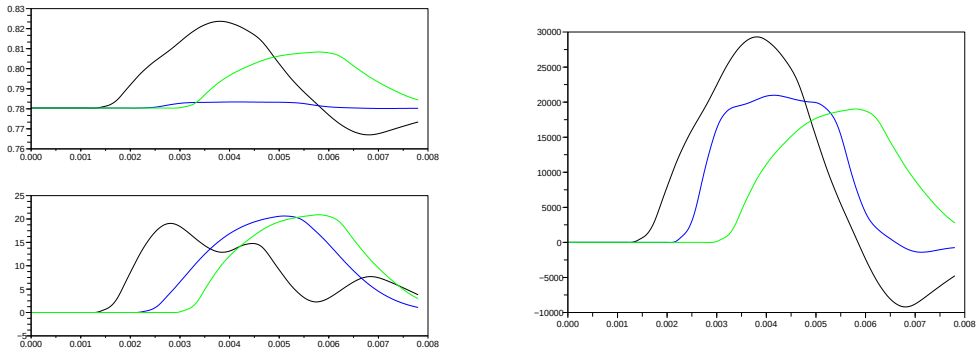

Fig. 3.9 Artery section (top left), blood flow rate (bottom left) and pressure (right) at points P, M, D for the variable compliance case.

The results depicted on Figure 3.9 show that the pressure wave is partially reflected at $z = a_1$, thus giving a more complex pressure profile downstream and also a decrease of the next pressure peaks. Note also that the propagation speed increases inside the disease portion while its section area remains almost constant.

3.2.3 Main results

3.2.3.1 The inverse problem with a constant compliance

The first inverse problem that is studied here concerns the case of an artery with a constant compliance. The objective is to find the optimal constant β that would allow the 1D model to fit as best as possible the corresponding 3D computation. In particular, it will corroborate or deny the formal expression previously given as the best choice for β.

To this aim, a preliminary 3D computation with a fluid structure model has first been done on an artery of the same type as the one used in the previous section and with the same pressure impulse. The 3D Navier Stokes equations with a linear Venant Kirchoff model for the structure have been solved with the C++ library *LifeV* (see [48] for more details). The results of this computation at a particular time are given on Figure 3.10.

Fig. 3.10 Solution of the 3D model at $t = 50.10^{-4}$ (left : fluid velocity, right : wall displacement)

To find the optimal value of β for the associated 1D model, an error-type cost function is defined. It uses the computed value with the 3D model of the section area A_{3D} and the volumic flux Q_{3D} for the three points P, M and D previously defined (see Figure 3.5) and at the times $t_i = i10^{-4}$ $(0 \leq i \leq 78)$. More precisely :

$$J_1(\beta) = \sum_{pts \in \{P,M,D\}} \sum_{i=0}^{78} \left(|A(t_i, pts) - A_{3D}(t_i, pts)|^2 + \frac{1}{10} |Q(t_i, pts) - Q_{3D}(t_i, pts)|^2 \right)$$

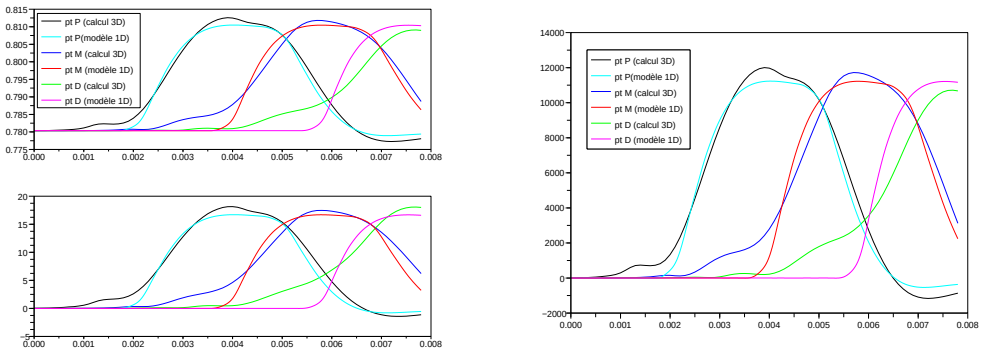

Fig. 3.11 Section area (top left), volumic flux (bottom left) and pressure (right) at points P, M and D for the 3D and the optimal 1D case, artery with constant compliance.

In [48], the same problem had been tackled by using a deterministic optimization method and by computing the gradient of J_1 with an adjoint formulation. It is solved here by using a

real valued Genetic Algorithm with 100 evaluations of the direct problem (5 individuals and 20 generations). As the shape of the function $\beta \to J_1(\beta)$ exhibits a convex behavior, both methods succeed to locate the global minimum of J_1, namely

$$\beta_{opt} = 0.5490284 * \beta_{formal} = 665077$$

It is interesting to notice that the optimal value of β which allows the 1D model to fit to the corresponding 3D model is far below the value issued from a formal derivation. A comparison between the values of section area, volumic flux and pressure issued from the 3D model and the 1D model with $\beta = \beta_{opt}$ at points P M and D is visible on Figure 3.11. It shows in particular that the 1D model can fit relatively well with the complex 3D model at a very lower computational cost.

3.2.3.2 The inverse problem with a variable compliance

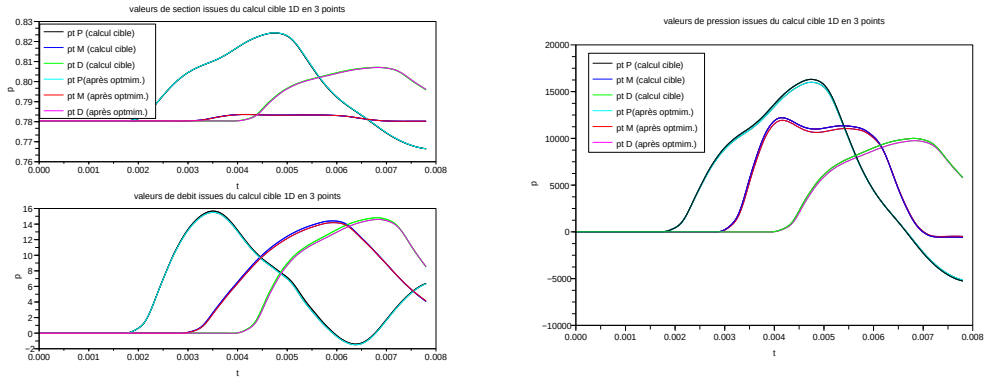

Fig. 3.12 Section area, volumic flux and pressure at points P, M and D for the synthetic data and the optimal 1D case, artery with variable compliance, cost function J_2.

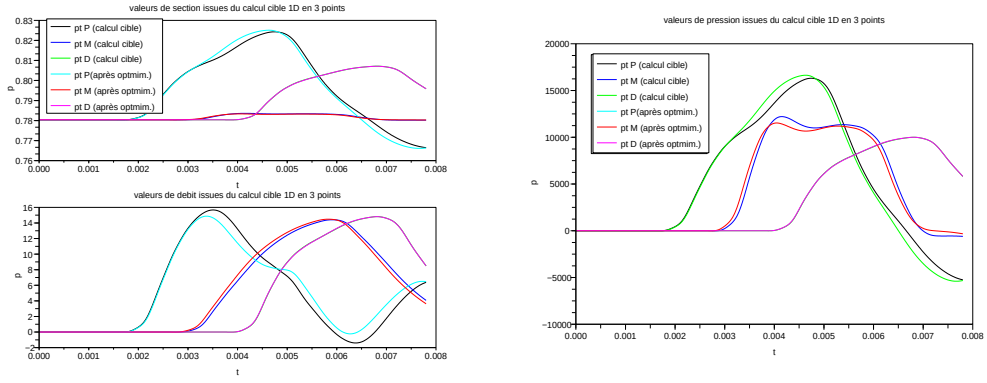

Fig. 3.13 Section area, volumic flux and pressure at points P, M and D for the synthetic data and the optimal 1D case, artery with variable compliance, cost function J_3.

The second inverse problem that is studied concerns the case of arteries having a compliance step that can be due to different reasons (stent, plaque,...). The objective now is is to determine the characteristics of this compliance step by looking at the values of the section area A and/or the volumic fluxe Q at different positions. In the present case, the synthetic data are issued from a direct computation of the 1D model already presented in a previous section (Test case 2).

In order to determine the amount of information needed to recover the correct parameters of the model, two test function have been tested. Both have four parameters as unknowns : the position of the compliance loss, a_1 and a_2, and the respective values, β_1 and β_2 of the function $z \to \beta(z)$ in both zones (see Figure 3.8). The two cost functions write respectively as :

$$J_2(a_1, a_2, \beta_1, \beta_2) = \sum_{pts \in \{P,M,D\}} \sum_{i=0}^{78} |A(t_i, pts) - A_{target}(t_i, pts)|^2 + \frac{1}{10} |Q(t_i, pts) - Q_{target}(t_i, pts)|^2$$

and

$$J_3(a_1, a_2, \beta_1, \beta_2) = \sum_{i=0}^{78} |A(t_i, D) - A_{target}(t_i, D)|^2$$

which means that the optimization is done with much less information in the case of J_3, namely the section area values down the compliance step.

Both optimization process have been done by using a real-valued Genetic Algorithm with less than 400 evaluations. In both cases the four parameters have been chosen in a very large domain. In particular, a_1 and a_2 are allowed to take all the values between 0 and 4 with $a_1 < a_2$.

In the case of the cost function J_2, the four parameters characterizing the function $z \to \beta(z)$ have been recovered with an excellent accuracy. It explains the perfect matching visible on Figure 3.12 of the values of the optimal 1D model with the synthetic data.

In the case of the cost function J_3, the situation is slightly different as the optimization process is only able to locate the position of the compliance step (that is a_1 and a_2) but not the exact amount of it. More precisely, the obtained value of β_1 matches the one used in the synthetic data but the value of β_2 is underpredicted by 50%. It can be observed on Figure 3.13 that the profile of the section area at point D is similar for both models while there exists some significant differences at point P, that is upstream the compliance step. However, in the future, such model may be able to help practioners for an efficient and quick diagnosis of arteries pathologies such as stenosis by using non invasive measurements.

3.3 Optimization with PDE constraints in a 3D space for car industry

Summary. In order to reduce their fuel consumption, the minimization of the drag coefficient of cars has become a major topic for car manufacturers. The developpement of fast and global optimization methods based either on hybridization of evolutionary algorithms with a local search process or on the use of surrogate models, has allowed only recently a first numerical and automatic approach for the drag reduction problem. The results obtained on a simplified geometry called Ahmed bluff body are presented here. They confirm the experimental analysis saying that the drag coefficient is very sensitive to the rear geometry of the car, because of the presence of separation and recirculation zones in this region, and thus can be largely reduced by shape optimization.

References : [Cha1], [Art5], [Art6], [Art7]

3.3.1 Objectives

The external shape of cars has always been evolving in the past, because of safety reasons, comfort improvement and also aesthetics considerations. The effect of these guidelines on car aerodynamics was not of prime importance during many years. This situation changed in the 70's with the breakthrough of the oil crisis. Indeed, it has been discovered at this time that the amount of the aerodynamic drag in the fuel consumption ranges between 30% during a urban cycle to 75% at a 120km/h cruise speed. Since this period, decreasing the fuel consumption of road vehicles became a major concern for car manufacturers. The ecological argument also appeared in the last decade to make this topic more crucial in the automotive research centers.

The process of drag creation and the way to control it has been first discovered experimentally. In particular, it has been found that the major amount of drag is due to the appearance of flow separation at the rear surface of cars ([50, 51]). Unfortunately, contrarily to the situation in aeronautics where it can be largely excluded from the body surface, this aerodynamic phenomena is an inherent situation for ground vehicles and can not be avoided. Moreover, the associated three-dimensional flow in the wake behind a car exhibits a complex 3D behavior and is very difficult to capture because of its unsteadiness and its sensitivity to the car geometry.

3.3.2 The drag reduction problem

3.3.2.1 The drag coefficient

A dimensionless coefficient, called drag coefficient and related to the drag force acting on a car or a bluff body, is defined in the following way :

$$C_d = \frac{F_d}{\frac{1}{2}\rho V^2 S} \tag{3.6}$$

In this expression, ρ represents the air density, V is the velocity of the car, S is the cross section area and F_d is the total drag force acting on the car in the longitudinal direction. Note that the drag force F_d can be decomposed into a sum of a viscous drag force and a pressure drag force. Examples of values of C_d for past or existing cars are presented in Table 3.1.

Car	C_d
Ford T (1908)	0.8
Hummer H2 (2003)	0.57
Citroen SM (1970)	0.33
Peugeot 407 (2004)	0.29
Tatra T77 (1935)	0.212

Tableau 3.1 Examples of drag coefficient C_d

It can be seen from this table that the drag coefficient of cars has been decreasing during the last century even though other considerations like comfort or aesthetics have also been taken into account to popularize a high drag model (see Hummer H2) or abandon a low drag model (see Tatra T77).

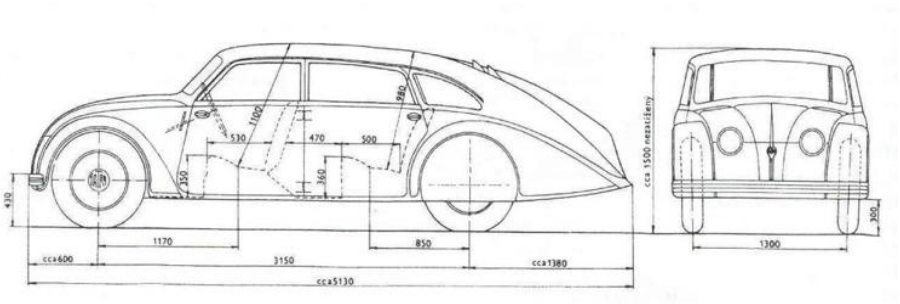

Fig. 3.14 Side and front view of Tatra T77 (1935, $C_d = 0.212$)

About the last example of Tatra T77 which had a remarkable low drag value of 0.212, a side and front view of this car is given in Figure 3.14. The short forebody compared to the very long tailored shape confirms the experimental observations stated in the previous section, saying that the separation zone at the slant and base area is the most important contribution to the total drag.

For a realistic car, Table 3.2 displays the repartition of the relative contribution of various elements on the total drag.

	percent of C_d
Upper surface	40%
Lower surface	30%
Wheels	15%
Cooling	10%
Others	5%

Tableau 3.2 Drag repartition on a realistic car

It shows in particular that 70% of the drag coefficient depends on the external shape. Such large value justifies the interest of a numerical modelization of the problem in order to find numerically innovative external shapes that will largely reduce the drag coefficient.

3.3.2.2 Numerical modelization

(i) The Navier Stokes equation

The incompressible Navier Stokes equations are governing the flow around the car shape. Denote S_c the car surface, G the ground surface and Ω a large volume around S_c and above G then, using the Einstein notation, the Navier Stokes equations write in the following way :

– Incompressibility :

$$\frac{\partial u_i}{\partial x_i} = 0 \quad \text{on } \Omega \tag{3.7}$$

– Momentum ($1 \leq j \leq 3$) :

$$\frac{\partial u_j}{\partial t} + \frac{\partial u_i u_j}{\partial x_i} = -\frac{1}{\rho}\frac{\partial p}{\partial x_j} + \frac{\partial}{\partial x_i}\left[\nu\left(\frac{\partial u_i}{\partial x_j} + \frac{\partial u_j}{\partial x_i}\right)\right] \quad \text{on } \Omega \tag{3.8}$$

where $u_j(t,x)$, $p(t,x)$ and ρ are respectively the flow velocity, pressure and density. The boundary conditions for the velocity are of Dirichlet type :

$$u_i = 0 \quad \text{on } S_c \cup G \quad \text{and} \quad u_i = V_\infty \quad \text{on } \partial\Omega \setminus (S_c \cup G) \tag{3.9}$$

As the Reynolds number is very high in real configurations, usually more than 10^6, a turbulence model must be added. This model must be of reduced computational cost in view of the large number of simulations, more than 100, that need to be done during the optimization process. That explains why the Large Eddy Simulation model can not be used here (see [56] and references herein for an example of the application of LES for a single computation around the Ahmed bluff body).

A Reynolds Averaged Navier Stokes (RANS) turbulence model which consists in averaging the previous equations (3.7) and (3.8), is chosen here. Denoting $\bar{u}_i$ the averaged velocity, a closure principle for the term $\overline{u_i u_j}$ has to be defined. The most popular way to do it leads to the well known $k-\epsilon$ model. In this model, the averaged equations (3.8) rewrite as :

$$\frac{\partial \bar{u}_j}{\partial t} + \frac{\partial \bar{u}_i \bar{u}_j}{\partial x_i} = -\frac{1}{\rho}\frac{\partial \bar{p}}{\partial x_j} + \frac{\partial}{\partial x_i}\left[(\nu+\nu_t)\left(\frac{\partial \bar{u}_i}{\partial x_j} + \frac{\partial \bar{u}_j}{\partial x_i}\right) - \frac{2}{3}\delta_{i,j}k\right] \quad \text{on } \Omega \tag{3.10}$$

where ν_t is called the eddy viscosity and is related to the turbulent kinetic energy k and its rate of dissipation ϵ by

$$\nu_y = C_\mu \frac{k^2}{\epsilon} \tag{3.11}$$

In this expression, C_μ is a constant and the new variables k and ϵ are obtained from a set of two equations (see [57]).

In the present configuration, it has been observed that the second order closure model called RSM with an adequate wall function gives better results than the $k-\epsilon$ method (see [55]). Despite the small computational overcost, of the order of 40%, this model will be prefered in the forthcoming simulations. A first example of such flow computation around a realistic car in given on Figure 3.15.

(ii) The cost function to minimize

The drag coefficient to be minimized is defined by the following expression :

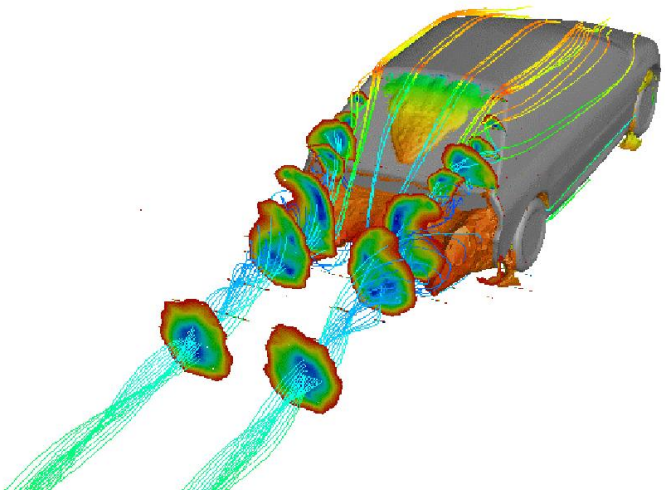

Fig. 3.15 Numerical flow field around a realistic car (Peugeot 206)

$$C_d = \frac{F_d}{\frac{1}{2}\rho V_\infty^2 S} \tag{3.12}$$

where ρ is the mass density, S the front surface, V_∞ the freestream velocity and F_x the longitudinal component of the aerodynamic force exerted on the car. The latter is obtained after a 3D turbulent Navier Stokes computation around the car :

$$\mathbf{F} = \iiint_{Shape} (P - P_\infty)\mathbf{n}dS + \iiint_{Shape} \rho V \frac{\partial V}{\partial y}\boldsymbol{\nu}dS \tag{3.13}$$

where $\mathbf{n}$ is the normal vector and $\boldsymbol{\nu}$ is the projection of the velocity vector to the element of shape dS.

The numerical computation of the drag coefficient that requires a full 3D turbulent Navier Stokes computation around the car is thus very costly, which explains the major difficulty of the related optimization problem.

3.3.3 Main results

3.3.3.1 Description of the test case

In order to test the global optimization methods on a realistic car drag reduction problem, a simplified car geometry has been extensively studied. It consists in minimizing the drag coefficient, also called C_d and defined in equation (3.12), of a simplified car shape with respect to the three geometrical angles defining its rear shape (see Figure 3.16) : the slant angle (called α), the boat-tail angle (β) and the ramp angle (γ). The forebody of the vehicle is fixed and corresponds to a shape near to an existing vehicle, namely the Xsara Picasso from Citroën. The objective is thus to find the best associated rear shape that will reduce the total drag coefficient of the car, without taking care of any any aesthetic considerations. As it has been observed experimentally on the Ahmed bluff body [51], it is expected that modifying the rear shape will lead to a very important drag reduction.

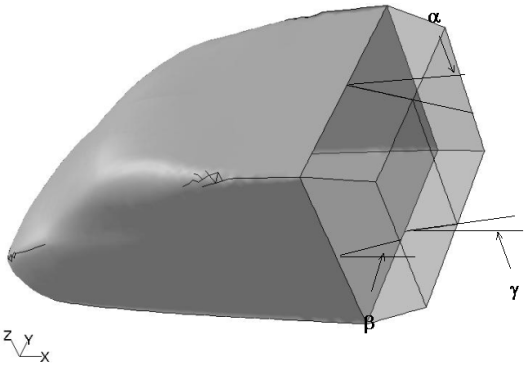

Fig. 3.16 3D car shape parametrized by its three rear angles α, β and γ

3.3.3.2 Details of the numerical simulation

An automatic optimization loop has been implemented and is summarized in Figure 3.17. This loop includes the following steps :

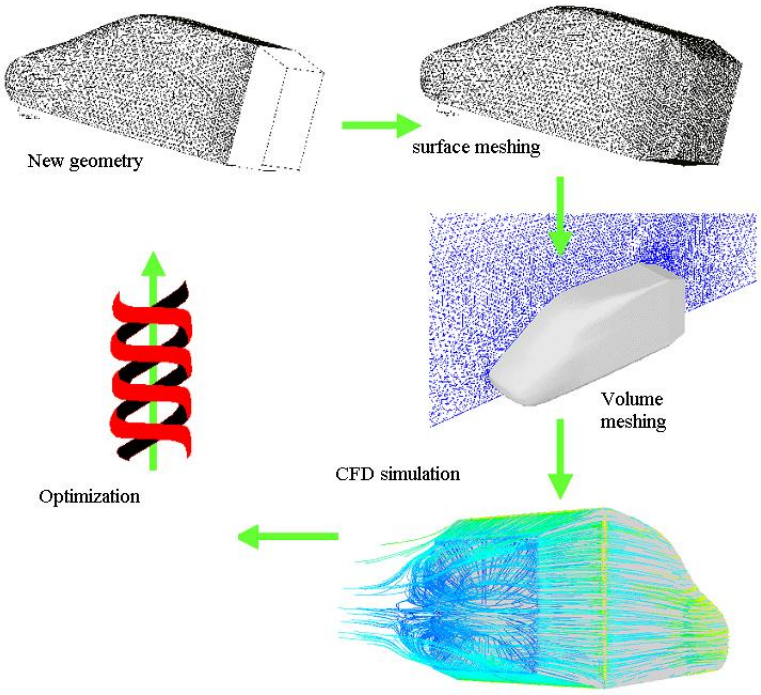

Fig. 3.17 General principles of the automatic optimization loop

(i) Car shape generation and meshing

The three rear angles are sought in the following intervals (in degrees) :

$$(\alpha, \beta, \gamma) \in [15, 25] \times [5, 15] \times [15, 25]$$

For any given geometry, the 3D-mesh around the car shape is generated with the commercial grid generator GAMBIT. It contains a total of approximately 6 millions of cells, both tetrahedrons and prisms. In order to simulate accurately the flow field behind the car which is responsible of the major part of the drag coefficient, the mesh is particularly refined in this region.

(ii) CFD simulation

The commercial CFD code FLUENT is used for the computation of the flow field around the car. The Reynolds number based on the body length (3.95m) and the velocity at infinity (40m/s) is taken equal to 4.310^6 like for the Ahmed experiment ([51]). The 6-equations turbulence model RSM is chosen as it gives better results in this case than the classical $k - \epsilon$ model (see [55]). The computation is performed until a stationary state is observed for the main aerodynamic coefficients which approximately takes 14 hours CPU time on a single processor machine. In order to achieve a reasonable computational time, parallel evaluations on a cluster of workstations have been done here.

(iii) Optimization method

Thwo different global optimization methods have been compared on this problem. The first one is a classical Genetic Algorithm (GA) with a population number N_p equal to 20, a crossover and a mutation coefficient respectively equal to 0.9 and 0.6. The second method consists in the same Genetic Algorithm but with fast and approximated evaluations, called AGA. Note that hybrid methods have also been tested on this problem but are not presented here as the AGA performs better. Contrarily to these three global optimization methods, it is worth mentioning that a pure deterministic method like BFGS fails to find the global drag minimum.

3.3.3.3 Numerical results

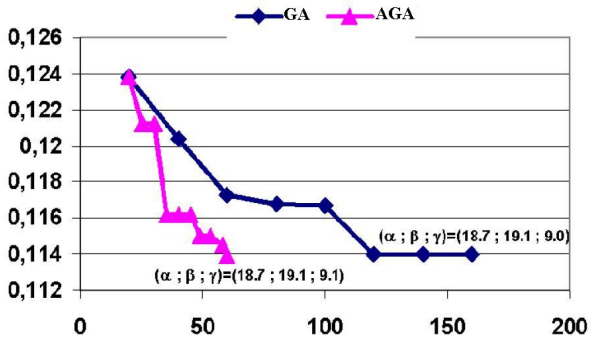

Fig. 3.18 Convergence history (best C_d vs. number of evaluations)

The convergence history of both optimization methods GA and AGA for the present drag reduction problem is depicted on Figure 3.18. This figure shows in particular that both methods have nearly reached the same drag value, namely 0.114, but with a different number of cost

function evaluations. More precisely, the AGA algorithm has permitted to reduce the exact evaluation number by a factor 2 compared to a classical GA, leading to the same proportional time saving.

The optimal angles obtained by both global optimization methods are nearly equal to $(\alpha, \beta, \gamma) = (18.7, 19.1, 9.0)$. These values have been experimentally validated in the Peugeot wind tunnel to be associated with the lowest drag value that can be reached with this particular forebody.

In order to understand more deeply the complex phenomenons involved in the variations of the drag coefficient, four characteristic shapes are presented in Table 3.3 and carefully studied.

shape	slant angle (α)	boat-tail angle (β)	ramp angle (γ)	C_d
(a)	21.1	24.1	14.0	0.1902
(b)	15.5	15.7	5.6	0.1448
(c)	16.9	17.7	11.3	0.1238
(d)	18.7	19.1	9.0	0.1140

Tableau 3.3 Four examples of characteristic shapes

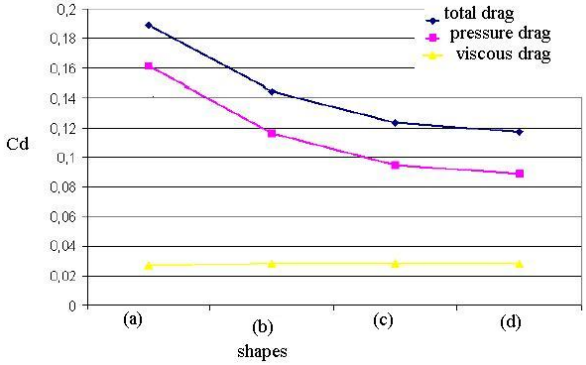

Fig. 3.19 Pressure and viscous part of drag for shapes (a) to (d)

The first shape, called (a), corresponds to a high drag configuration whereas shapes (b), (c) and (d) correspond to low drag configurations with an increasing value of slant and boat-tail angles. More precisely, shape (c) corresponds to the best shape obtained after the first generation of the GA whereas shape (d) is the best shape obtained in the whole range of admissible angles. Compared to shape (a), note that value of the drag coefficient of shape (d) is almost divided by a factor two even if both shapes are actually not very different which confirms the high dependance of C_d on the rear shape.

Figure 3.19 displays for the four chosen configurations, the relative part of the pressure drag and the viscous drag in the value of the drag coefficient C_d. It is worth noticing that the pressure drag represents the major contribution to the total drag and also that the viscous drag remains almost constant for all cases. In particular, a higher pressure at the rear of the car will automatically reduce the drag. To see more precisely the topology and the pressure values of the wake flow, Figure 3.20 depicts for shapes (a) to (d) the isosurface of null longitudinal velocity colored with the pressure coefficient. The latter corresponds to an dimensionless pressure value and is given by :

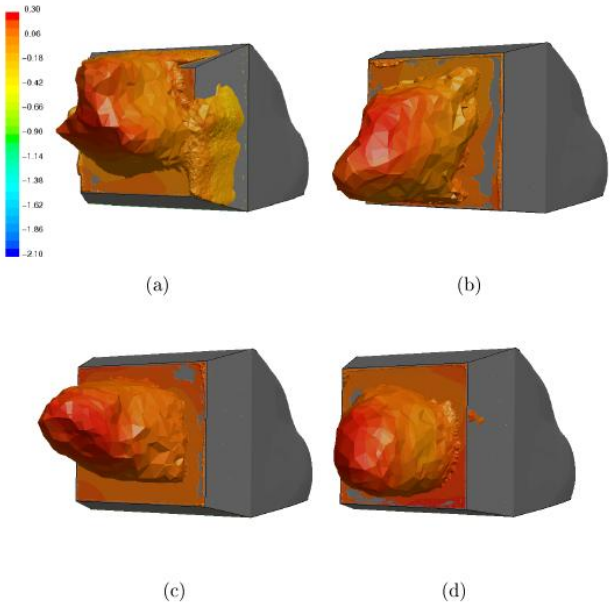

Fig. 3.20 Isosurface of null longitudinal velocity colored with pressure coefficient for shapes (a) to (d)

$$C_p = \frac{P - P_\infty}{\frac{1}{2}\rho V_\infty^2} \tag{3.14}$$

It can be seen in particular on shapes (a) and (b) that too high, respectively too low, slant and boat-tail angles will not generate a sufficient pressure level at the rear of the vehicle, thus increasing the pressure drag. On the contrary, intermediate and similar values of these two angles, coupled with a low ramp angle as it is the case for shapes (c) and (d), will improve the recompression at the car base. Note also that the optimal shape (d) is associated to a very narrow and regular recirculation bulb. All these observations corroborate the qualitative trends well known by car engineers since the experiments done by Morel [50] and Ahmed [51].

3.4 Optimization with PDE constraints in a 3D space for medicine

Summary. In this section, various test cases are presented to show how optimization can improve the placement of the electrodes of a pacemaker. A robust cost function based on the depolarization delay of the disease heart is in particular introduced. The obtained result show how a rather good ECG can be recovered, even with only one electrode, after an optimization of its positioning.

References : [Art12], [Proc3], [Proc4].

3.4.1 Objectives

The heart is located between the lungs and consists of four parts, the right and left atria and ventricles. The function of the heart involves pumping blood from the lung and the body and ejecting it towards the body allowing the organs to operate. This function is the result of a contraction–relaxation process induced by an electrical impulse moving across the heart. The electrical signal is first induced in the sinus node, the natural pacemaker, then propagates through the atria and reaches the ventricles through the atrioventricular (A-V) node, see Figure 3.21. In the ventricles, the propagation is led by the bundle of His causing a wavefront which propagates by a cell–to–cell activation. In each cell, a depolarization phase occurs corres-

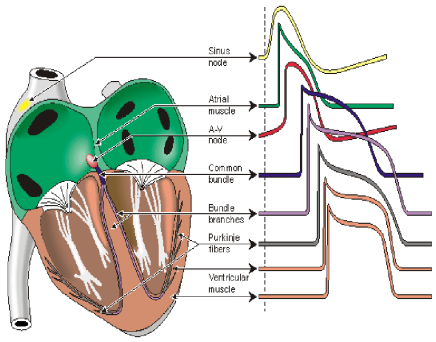

Fig. 3.21 Potential profiles at various points

ponding to the inflow of sodium ions (causing the electrical activation) followed by a plateau phase, and then by a repolarization phase corresponding to the outflow of potassium ions. This phenomenon is illustrated in Figure 3.21 by the representation of the potential action in different types of cardiac cells.

The electrical activity of the cell membranes is generally modelled by the so–called bidomain equations [58] in which the current term due to ionic exchanges can be simulated by the Mitchell and Schaeffer model [59].

The electrical conduction of heart may be defective causing the heartbeat to be too fast, too slow or irregular. Some pathologies, as for example sinus node dysfunction or bundle branch block are treated with an artificial pacemaker which is used to help the heart to recover a quasi–normal electrical activity. A pacemaker consists of a small battery and electrodes transmitting the electrical impulse. Though today pacemakers give good results, certain questions still arise. How many electrodes should be set ? Where the electrodes should be placed ? When the electrodes should act ? Many experiments are led to give answers to these questions, see [60] and

references therein. As experimental measurements are difficult to obtain, numerical simulations may contribute to a better understanding.

3.4.2 Modelling of the heart electrical activity

3.4.2.1 The bidomain model

At the microscopic level, the cardiac muscle, denoted by Ω_H, is made of two distinct and intricate media : the intra and extra-cellular media, respectively called Ω_{Hi} and Ω_{He}, that are separated by a surface membrane Γ_H (see Figure 3.22).

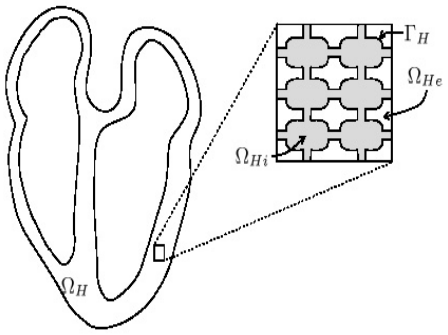

Fig. 3.22 Simplified view of the heart at macro/microscopic level.

After a homogenization process, the corresponding electrical potentials ϕ_i and ϕ_e and the transmembrane potential

$$V_m(t,x) = \phi_i(t,x) - \phi_e(t,x) \tag{3.15}$$

are defined on the entire domain $x \in \Omega_H$ and satisfy the so–called bidomain model [58], on $[0,T] \times \Omega_H$:

$$A_m \left(C_m \partial_t V_m + I_{\text{ion}}\right) - \text{div}(\sigma_i \nabla V_m) = \text{div}(\sigma_i \nabla \phi_e)\,, \tag{3.16}$$

$$\text{div}(\sigma_i \nabla \phi_i) = -\text{div}(\sigma_e \nabla \phi_e)\,, \tag{3.17}$$

with the following boundary condition on the heart boundary $\partial\Omega_H$:

$$\sigma_i \nabla \phi_i \cdot n = \sigma_e \nabla \phi_e \cdot n = 0\,, \tag{3.18}$$

where n denotes the outward unit normal at $x \in \partial\Omega_H$.

Finally an initial condition is prescribed :

$$V_m(0,x) = V_m^0(x) \quad \text{ in } \Omega_H\,. \tag{3.19}$$

In this model, the parameters A_m, C_m, σ_i and σ_e respectively denote the average rate of membrane surface per volume area, the membrane capacity and the intra and extracellular conductivity tensors. Note that the presence of electrodes is modelled here by adding a local source term in (3.16).

The current term due to ionic exchanges, I_{ion}, is evaluated with the help of the physiological model of Mitchell and Schaeffer [59] :

$$I_{\text{ion}} = -\frac{w}{\tau_1} V_m^2 (1 - V_m) + \frac{V_m}{\tau_2}\,, \tag{3.20}$$

where the auxiliary variable w satisfy the following ODE :

$$\frac{dw}{dt} = g(V_m, w)\,, \quad \text{with} \quad g(V_m, w) = \begin{cases} \frac{w-1}{\tau_3} & \text{if } V_m < V_g\,, \\ \frac{w}{\tau_4} & \text{if } V_m > V_g\,, \end{cases} \tag{3.21}$$

and $\tau_1\,, \tau_2\,, \tau_2\,, \tau_3\,, \tau_4$ and V_g are given parameters.

The model (3.16)–(3.21) is usually used when the heart is isolated. In order to derive an ECG, this model is coupled with a model of the electrical activity of the surrounding tissues. To this end, we assume that the interface between the heart and the extra–cardiac region is divided into the endocardium Γ_{endo} and the epicardium Γ_{epi}. Then, the coupling we consider is

$$\begin{cases} R_p \sigma_e \nabla \phi_e \cdot n = R_p\, C_p \frac{\partial(\phi_T - \phi_e)}{\partial t} + (\phi_T - \phi_e) & \text{on } \Gamma_{\text{epi}} \\ \sigma_e \nabla \phi_e \cdot n = \sigma_T \nabla \phi_T \cdot n & \text{on } \Gamma_{\text{endo}}\,, \end{cases} \tag{3.22}$$

where ϕ_T denotes the potential in the torso domain, R_p and C_p are given parameters. We refer to [62] for more details.

3.4.2.2 Pathologic case

The pathology we consider here is called left bundle branch block. In such situation, the electric signal can not be propagated by the bundle of His in the left ventricle, consequently the depolarization process occurs with delay causing asynchronous contraction–decontraction. In the previous bidomain model, it is simulated by an absence of initial natural stimulation in the left ventricle in equation (3.19).

In order to help the heart to recover its normal electrical activity, a well known surgery device, called pacemaker, is used. It acts through the application of a certain number of electrodes located at the heart surface that are able to give a local electrical impulse. In the previous bidomain model, the electrodes act like a local (in space and time) current volumic source term in the right hand side of the equation (3.16).

3.4.3 Main results

3.4.3.1 Description of the cost function

We investigate two different cost functions to optimize the positioning of the electrodes of a pacemaker on a disease heart. We first consider a cost function which takes into account the delay of a characteristic depolarization time, namely

$$J_1 = t_d - t_{d,target}\,, \tag{3.23}$$

where t_d represents the first time for which 95 per cent of the whole heart is depolarized :

$$t_d = \inf\{t \geq 0, \quad \text{Volume}(\Omega_t) \geq 0.95\, \text{Volume}(\Omega_H)\}\,,$$

with :

$$\Omega_t = \{x \in \Omega_H, \quad V_m(t,x) > V_s\}\,.$$

and $t_{d,target}$ denotes the same value for the corresponding healthy heart.

The second cost function we consider is based on the behavior of the ECG during the depolarization phase :

$$J_2 = \|D - D_{target}\|_{L^2(0,T)}\,, \tag{3.24}$$

where D is the so–called first lead of the ECG given by

$$D = \phi_T(L) - \phi_T(R)\,,$$

where L and R are two points of measure located on the left and right arm. As above, D_{target} denotes the same value for the corresponding healthy heart.

3.4.3.2 Description of the test case

The simulations are performed on a simplified geometry which contains ventricles only, see Figure 3.23.

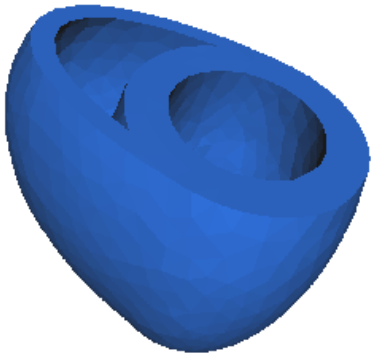

Fig. 3.23 A simplified heart geometry Ω_H.

The domain, closed to a human heart, is analytically defined through its boundary, made of the union of four truncated ellipsoids :

$$(\tfrac{x}{a_{iL}})^2 + (\tfrac{y}{b_{iL}})^2 + (\tfrac{z}{c_{iL}})^2 = 1, \quad (\tfrac{x}{a_L})^2 + (\tfrac{y}{b_L})^2 + (\tfrac{z}{c_L})^2 = 1\,,$$

with $\{a_{iL}\,, b_{iL}\,, c_{iL}\,, a_L\,, b_L\,, c_L\} = \{2.72, 2.72, 5.92, 4, 4, 7.2\}$ cm for the left ventricle internal and external boundary respectively, and

$$(\tfrac{x}{a_{iR}})^2 + (\tfrac{y}{b_{iR}})^2 + (\tfrac{z}{c_{iR}})^2 = 1, \quad (\tfrac{x}{a_R})^2 + (\tfrac{y}{b_R})^2 + (\tfrac{z}{c_R})^2 = 1\,,$$

with $\{a_{iR}\,, b_{iR}\,, c_{iR}\,, a_R\,, b_R\,, c_R\} = \{7.36, 3.36, 6.2, 8, 4, 6.84\}$ cm for the right ventricle. All these ellipsoids are restricted to the half space $z \leq 2.75$.

Note that the pathology considered here, is called a left bundle branch block for which only the right ventricle is initially stimulated. In this case, the electrodes can be placed in the atria

and/or in the ventricles. As we only simulate here the ventricles, we seek for the best positioning of the electrodes in the internal surface of the left ventricle.

3.4.3.3 Numerical results

We choose the conductivities in (3.16) such that the anisotropy of the fibers in the myocardium are taken into account, namely $\sigma_i = \alpha_i^t(I - d_f \otimes d_f) + \alpha_i^l(I - d_f \otimes d_f)$ and $\sigma_e = \alpha_e^t(I - d_f \otimes d_f) + \alpha_e^l(I - d_f \otimes d_f)$, where d_f is the direction of the fibers, I the identity matrix in R^3 and $\alpha_i^t = 5\,10^{-3}, \alpha_i^l = 1.5\,10^{-1}, \alpha_e^l = 1.\,10^{-1}$ and $\alpha_e^t = 7.5\,10^{-3}$. The parameters in (3.16)–(3.21)are choosen as follows : $A_m = C_m = 1$, $\tau_1 = 0.45$, $\tau_2 = 9$, $\tau_3 = 150$, $\tau_4 = 100$, $V_g = 0.13$ and R_p and C_p are choosen sufficiently small. The intensity of the initial stimulation equals 0.5 mV during 10 ms. The artificial stimulations have the same intensity as the initial stimulation and hold during 40 ms. As we are interested in the depolarization phase only, the final time of computations is actually equal to 100 ms whereas the total duration of depolarization–repolarization process is approximately 300 ms.

The domain Ω_H is discretized with tetrahedra for a total number of nodes equal to 12921. The ionic current is solved by the *cvode*[1] solver, an appropriate solver for stiff nonlinear systems of ODE. The bidomain problem (3.16)–(3.21) is approximated by a piecewise finite elements scheme in space and by a second order backward differences scheme in time. The simulations are done with the C++ library *LifeV*[2].

A number of 30 individuals in taken for the GA population in the case of the optimization of the positioning of one electrode. A number of 10 generations is then needed to achieve a near optimal solution. Note that a similar computation has also been done on a finer grid of the heart muscle by using the AGA algorithm and a parallel implementation on a 13 proc. cluster and has lead to the same results.

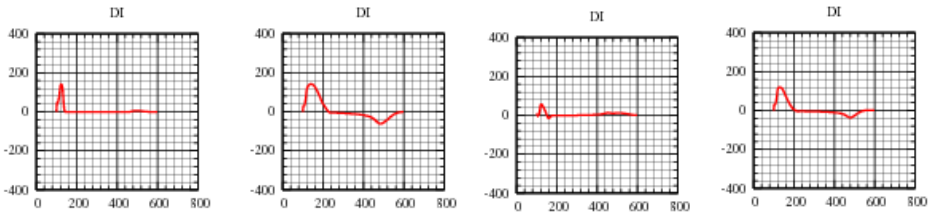

Fig. 3.24 The first lead (DI) of the ECG in the reference case, the pathologic case, the pathologic case with one electrode when J_1 is used and when J_2 is used (from left to right).

We first present the results obtained by using the cost function J_1. In this case the isolated model (3.16)–(3.21) is used to simulate the electrical activity of the heart. In the pathological case $J_1 = 73$ ms whereas this delay is reduced to $J_1 = 20.75$ ms when an electrode is placed at the optimal point which actually corresponds to the value

$$(x, y, z) = (3.71, 0.024, -2.03)\,.$$

When we use the cost function J_2, the coupled model (2)–(8) is used and the optimal positionning of the electrode is the following :

[1] http ://llnl.gov/casc/sundials

[2] http ://www.lifev.org/

$$(x, y, z) = (-1.29, 1.68, -3.69)\,.$$

Note that for this position, the delay in the depolarization process, namely J_1, is far from being optimal as it equals 64.75 ms. These results show that according to the cost function, the optimal positionning of the electrode can be very different.

Figure 3.24 shows the first lead of ECG, respectively in the reference case, the pathologic case and the pathologic case after an optimization with J_1 and J_2.

It is natural that the recovery of this particular lead of the ECG is more efficient with the J_2 optimization, in view of its definition in (3.24). However, the results obtained with the J_1 optimization also lead to a good ECG recovery even if it is based on a different criteria. Moreover, for the corresponding optimal point, all the other leads of the ECG also perform well. It thus seems to indicate that the J_1 optimization is the more interesting and robust criteria for the optimization of the positioning of the electrodes of a pacemaker. Note also that a computation with two electrodes, not shown here, has allowed the cost function J_1 to decrease still more but to a lesser extent.

3.5 Other examples

3.5.1 Optimization of a stent shape

Reference : [Proc6].

3.5.1.1 Objectives

Cardiovascular diseases are the first cause of death in Europe. For two decades, they constitute an important subject of clinical investigations and academic studies. The well known stenosis pathology — reduction of the vascular lumen of an artery— affects the dynamics of the blood flowing through arteries and may even obturate them.

An appropriate procedure to eradicate this constriction is a balloon angioplasty, and/or a stent placement ([63], [65]). In the latter procedure, a stent is transported by a catheter, known as a stent delivery device, to the defective site in the artery and then expanded radially by the balloon to dilate the site (see Figure 3.25).

Though this method is commonly used by practitioners, the stent treatment is not a perfect solution and is often associated with complications such as restenosis. Indeed, numerous clinical studies describe the vessel damage during stent implantation and thereof the arterial wall growth over the wire mesh of the prothesis for about 20-30% of the patients who receive it.

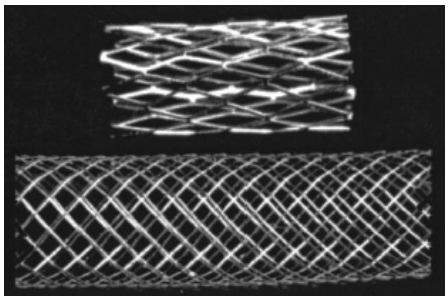

Fig. 3.25 A balloon expandable stent.

Many numerical simulations have been done, by following various approaches, to understand why restenosis occurs. Some authors have carefully studied the two-dimensional ([63], [64], [65], [47], [66]) or even three-dimensional ([68]) blood flow behavior through stented arteries. Others have focused on the mechanical properties of the stent ([67]) or on chemical aspects of coated stents ([69]).

We adopt, here, the fluid-structure approach to describe the problem. We then couple equations with a stochastic optimization process in order to define optimal stent designs. More precisely, we are seeking with the best three geometric parameters of a simplified two-dimensional stent, namely the strut spacing l, the strut height h and the strut width w that could reduce blood stagnation and also fluid swirl. To perform optimization, a multicriteria genetic algorithm has been used.

3.5.1.2 Main results

The most important criteria to fulfill for designing optimal stents that has been obtained is the following : in all cases, the ratio $r = l/h$ has to be chosen greater than r_u. It corresponds to a situation where the two recirculation areas before and after each strut are separated. Moreover, a higher ratio, that can be raised up to 20 in our study, is not always preferable. Note also that the strut width w only plays a secondary role compared to l and h in the optimization process. It will thus be adjusted by the designer at its convenience. Another important observation coming from this work is the relative independence on the design results of some simplificatory hypotheses that can be made during the modelling phase, such as the steady flow hypothesis or the absence of fluid-structure interaction.

3.5.2 Optimization of a blade shape

Reference : [Cha1], [Art10].

3.5.2.1 Objectives

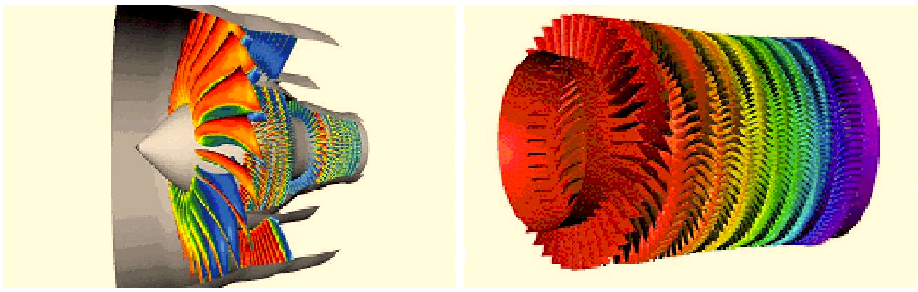

Fig. 3.26 Blades in the fan (left) and the high pressure compressor module (right)

In a turboreactor, the blades, which represent a big amount of an engine price (nearly 35%), are designed in order to create and control the aerodynamic flow through the engine (see Figure 3.26).

The design of the blades in the high pressure compressor module is optimized in order to minimize the mechanical efforts applied on them. Actually, it represents only a first step in the field of blades optimization as, for a high pressure compressor designer, increasing the isentropic efficiency of the compressor is the main target. Nevertheless, this goal can not be achieved regardless other engine features. Among them is the stall margin. This aerodynamic instability phenomena consists in the stall of the flow around the blades. This leads to backward flow inside the compressor and can result in engine shutdown, overtemperature in the low pressure turbine, high level of vibration or blade out. To prevent such events, the designer will have to increase the compressor pressure ratio for low mass flow rates.

3.5.2.2 Details of the computation

A 3D blade can be broken down into a set of several 2D airfoils profiles. The different airfoils are linked to the original blade through the stacking law (see Figure 3.27). Each airfoil can then be described by a set of design parameters which reflect physical phenomenon that can be seized by the human designer. Figure 3.27 shows some of common design parameters of the 2D profiles such as chord (c), maximum thickness value (e), upstream and downstream skeleton angles (β_1 and β_2), stagger angle (γ). In the presented case, theses parameters are kept fixed whereas the parameters to optimize, on the number of six, are all associated to the stacking law.

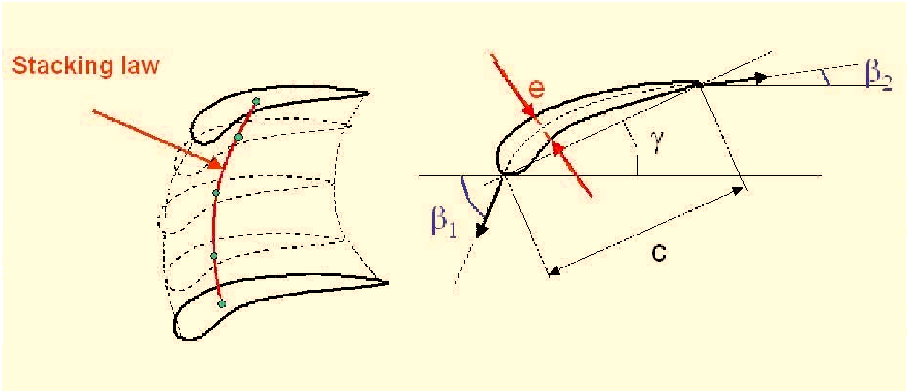

Fig. 3.27 Design parameters of a 3D blade

In order to minimize the mechanical efforts on the blade, the associated function to minimize is equal to the maximal value on 2D profiles of the Von Mises constraints (see [70] for more details on this criteria). Such problem is highly non linear, has a large number of constraints, many local minima and is also time consuming.

3.5.2.3 Obtained results

The Adaptive Hybrid Method (AHM) method with a reduced clustering strategy has been used here to solve the blade optimization problem described above. Note in particular that constraints are handled with a penalization term whereas the gradients are approximated by finite differences.

Optimization method	number of evaluations	best obtained value
Commercial code	460	163.5
AHM	480	158.6

Tableau 3.4 The blade optimization problem, performances comparison

The results are compared on Table 3.4 with those obtained with a commercial optimization platform based on a pure stochastic algorithm. It can be seen that for the same simulation time (approximately 80 hours CPU), the Adaptive Hybrid Method overperforms the commercial code . Indeed, even if the relative decrease obtained on the cost function appears to be small (3% approximately), it actually represents a significant improvement for the blade design. Note

that such very interesting optimal value had never been achieved previously, even after many independent runs of the commercial code.

Bibliographie

[1] C. Cercignani, R. Illner, M. Pulvirenti, *The Mathematical Theory of Dilute Gases*, Springer-Verlag, New York (1994).

[2] H. Spohn, The Lorentz flight process converges to a random flight process, *Comm. Math. Phys.*, 60, 277–2990 (1978).

[3] L.A. Bunimovich and Ya. G. Sinai, Markov Partitions of Dispersed Billiards, *Commun. Math. Phys.* 73, 247–280, (1980) ; *and* Statistical properties of the Lorentz gas with periodic configurations of scatterers, *Commun. Math. Phys.* 78, 479–497 (1981).

[4] C. Boldighrini, L.A. Bunimovich, and Ya. G. Sinai, On the Boltzmann equation for the Lorentz gas, *J. Stat. Phys.* 32 (3), 477–501, (1983).

[5] N. Chernov, New proof of Sinai's formula for the entropy of hyperbolic billiard systems, applications to Lorentz gases and Bunimovich stadium, *Funct. Anal. and Appl.*, 25 (3), 204–219 (1991).

[6] P. Bleher, Statistical properties of two dimensional periodic Lorentz gas with infinite horizon, *Journal of Stat. Phys.*, 66 (1/2), 315-373 (1992).

[7] F. Golse, Transport dans les milieux composites fortement contrastés, le modèle du billard, *Ann. Inst. H. Poinc. Phys. Théor.*, 61, 381–410 (1994).

[8] P. Garrido, G. Gallavotti, Billiards correlation functions, *Journal of Statistical Physics*, 76, 549–586 (1994).

[9] N. Chernov, Entropy, Lyapunov Exponents and Mean Free Path for Billiards ; *preprint* (1996).

[10] J. Bourgain, F. Golse, B. Wennberg, On the distribution of the free path length for the periodic Lorentz gas, *Comm. Math. Phys.*, 1990, 491–508 (1998).

[11] F. Pene, Rates of convergence in the CLT for two-dimensional dispersive billiards, *Communications in Mathematical Physic*, 225 (1), 91–119 (2002).

[12] F. Pene, Asymptotic of the number of obstacles visited by the planar Lorentz gas, to appear in *Discrete and Continuous Dynamical Systems* (2008).

[13] P. Billingsley, *Probability and Measure*, 2nd edition, Wiley, New York, (1986).

Section 1.2 :

[14] F. Odar, W.S. Hamilton, Forces on a sphere accelerating in a visous fluid, *Journal of Fluid Mech.*, 18 (2), 307–314 (1964).

[15] S. Boraas, Modeling slag deposition in the Space Shuttle SRM, *J. of Spacecraft* (1994).

[16] P. Liaw, Y.S. Chen, Particulate multi-phase flow field calculation with combustion/breakup models for solid rocket motors, *AIAA paper*, 94/2780 (1994).

[17] B. Maury, Direct Simulations of 2D Fluid-Particle Flows in Biperiodic Domains, *Journal of Computational Physics*, 156, 325-351 (1999).

[18] J. Dupays, Y. Fabignon, G. Lavergne, J.-L. Estivalezes, Ph. Villedieu, Two phase flows in solid rocket motor chambers due to aluminum particles into the propellant, *Progress in Astronautics and Aeronautics*, 185 (2000).

[19] Y. Fabignon, J.-F. Guéry, F. Godfroy, P. Le Helley , J. Hylkema, L. Jacques, G. Lavergne, Ph. Villedieu, Slag accumulation in large segmented solid boosters with a submerged nozzle, *Second European Conference on Launcher Technology*, Rome (2000).

Chapitre 2 :

[20] J. Holland, *Adaptation in Natural and Artificial Systems*, University of Michigan Press, Ann Arbor (1975).

[21] Goldberg D.E., *Genetic Algorithms in Search, Optimization, and Machine Learning*, Addison-Wesley (1989).

[22] R. Cerf, Une théorie asymptotique des Algorithmes Génétiques, *thèse de Doctorat*, Univ. Montpellier (1994).

[23] Z. Michalewicz, M. Schoenauer, Evolutionary Algorithms for Constrained Parameter Optimization Problems, *Evolutionary Computation*, 4 (1), 1–32, (1996).

[24] Z. Michalewicz, *Genetic Algorithms + Data Structures = Evolution Programs*, Springer-Verlag (1999).

[25] K. Miettinen, Pekka Neittaanmäki, M. M. Mäkelä, and Jacques Périaux, *Evolutionary Algorithms in Engineering and Computer Science : Recent Advances in Genetic Algorithms, Evolution Strategies, Evolutionary Programming, Genetic Programming and Industrial Applications*, Wiley (1999).

[26] Beyer H.G., Schwefel H.P., *Evolution Strategies*, Kluwer Academic Publisher (2002).

[27] A. Auger, C. Le Bris, M. Schoenauer, Rigorous analysis of some simple adaptive ES, *INRIA report*, RR4914 (2003).

[28] H. Ulmer, F. Streichert, A. Zell, Optimization by Gausian Processes assisted Evolution Strategies, *Proceedings of the 2003 Congress on Evolutionary Computation*, 1, IEEE Press, 692-699 (2003).

[29] C. Poloni, Hybrid GA for multi objective aerodynamic shape optimization, *Genetic algorithms in engineering and computer science*, John Wiley and Sons, 33, 397-415 (1995).

[30] J.M. Renders and S.P. Flasse, Hybrid methods using genetic algorithms for global optimization, *IEEE Transactions on systems, man and cybernetics*, 26, 243-258 (1996).

[31] Vicini A. and Quagliarella D. : Airfoil and wing design through hybrid optimization strategies. *AIAA paper* (1998).

[32] F. Espinoza, B. Minsker and D.E. Goldberg, A self adaptive hybrid genetic algorithm, *Proceedings of GECCO 2001*, Morgan Kaufmann Publishers (2001).

[33] M-R. Chen, Y.-Z. Lu, Q. Luo, A novel hybrid algorithm with marriage of particle-swarm optimization and extremal optimization, *Optimization community e-print* (2007).

[34] K.C. Giannakoglou, Acceleration of GA using neural networks, theoretical background, GA for optimization in aeronautics and turbomachinery, *VKI Lecture Series* (2000)

[35] Y. Jin, M. Olhofer and B. Sendhoff, A framework for evolutionary optimization with approximate fitness functions, *IEEE Transactions on Evolutionary Computation*, 6, 481-494 (2002)

[36] Y.S. Ong, P.B. Nair and A.J. Keane, Evolutionary Optimization of Computationally Expensive Problems via Surrogate Modeling, *AIAA Journal*, 41, 687-696 (2003)

[37] Y.S. Ong, P.B. Nair, A.J. Keane and K. W. Wong, Surrogate-Assisted Evolutionary Optimization Frameworks for High-Fidelity Engineering Design Problems, Knowledge Incorporation in Evolutionary Computation, *Studies in Fuzziness and Soft Computing Series*, Springer Verlag, 307-331 (2004).

[38] Y. Jin, A survey on fitness approximation in evolutionary computation, *Journal of Soft Computing*, 9, 3-12 (2005)

[39] B. Abou El Majd, J.-A. Desideri and R. Duvigneau, Multilevel strategies for parametric shape optimization in aerodynamics, *European Journal of Computational Mechanics*, 17 (1-2) (2008).

[40] E. Taillefer, Méthodes d'optimisation d'ordre zéro avec mémoire en grande dimension : application à la compensation des aubes de compresseurs et de turbines, *thèse de Doctorat*, MIP Toulouse (2008).

Section 3.1 :

[41] T. Erdogan, Fiber Grating Spectra, *J. of lightwave technology.*, 15 (8), 1277-1294 (1997).

[42] M. Ibsen, M.K. Durkin, M.J. Cole and R.I. Laming, Sinc-Sampled Fiber Bragg Gratings for Identical Multiple Wavelength Operation. *IEEE Photonic Technology Letter*, 10 (6), 842-844 (1998).

[43] J. Skaar and K.M. Risvik, A Genetic Algorithm for the Inverse Problem in Synthesis of Fiber Gratings. *J. of Lightwave Technology*, 16(10), 1928-1932 (1998).

[44] J.E. Rothenberg, H. Li, Y. Li, J. Popelek, Y. Sheng, Y. Wang, R.B. Wilcox and DJ. Zweiback, Fiber Bragg Gratings and Phase-Only Sampling for High Channel Counts. *IEEE Photonic Technology Letter*, 14(9), 1309-1311 (2002).

Section 3.2 :

[45] A. Quarteroni, L. Formaggia, Mathematical modelling and numerical simulation of the cardiovascular system, Modelling of Living Systems, *Handbook of Numerical Analysis*, 19, Elsevier Science, Amsterdam (2002).

[46] L. Formaggia, F. Nobile and A. Quarteroni, A One Dimensional Model for Blood Flow : Application to Vascular Prosthesis, *Lecture Notes in Computational Science and Engineering*, 19, 137-153 (2002).

[47] A. O. Frank, P. W. Walsh and J. E. Moore Jr, Computational Fluid Dynamics and Stent Design, *Artificial Organs*, 26(7), 614–621, Blackwell Publishing, Inc. (2002).

[48] V. Martin, F. Clément, A. Decoene and J.F. Gerbeau, Parameter identification for a one-dimensional blood flow model, *Esaim Proc.*, 14, 174-200 (2005).

[49] V. Melicher, V.A. Gajdosík, A numerical solution of a one-dimensional blood flow model-moving grid approach,*Journal of Comput. and Applied Math.*, 215 (2), (2008).

Section 3.3 :

[50] T. Morel : Aerodynamic drag of bluff body shapes characteristic of hatch-back cars, *SAE technical paper*, series 780267 (1978).

[51] S.R. Ahmed, R. Ramm, G. Faltin, Some salient features of the time averaged ground vehicle wake, *SAE technical paper*, series 840300 (1984).

[52] T. Han : Computational anlysis of three-dimensional turbulent flow around a bluff body in ground proximity, *AIAA journal*, 27 (9), (1988).

[53] C.J. Sagi, T. Han, D.C. Hammond : Optimization of bluff body for minimum drag in ground proximity, *AIAA journal*, 30 (4), (1992).

[54] P. Gillieron, F. Chometon, Modelling of stationary three dimensional separated flows around an Ahmed reference model, *ESAIM proceedings*, 7, (1999).

[55] F.T. Makowski, S-E Kim, Advances in external-aero simulation of ground vehicles using the steady RANS equations, *SAE technical paper*, series 010484 (2000).

[56] G. Franck, N. Nigro, M. Storti, J. d'Elia, Numerical simulation of the Ahmed vehicle model near-wake, preprint, to appear in *Int J Num Meth Fluidextracts*.

[57] Mohammadi B., Pironneau O.,*Analysis of the k-epsilon turbulence model*, John Wiley and Sons, 1994.

Section 3.4 :

[58] C.S. Henriquez Simulating the electrical behavior of cardiac tissue using the bidomain model. *Critical Reviews in Biomedical Engineering*, 21(1), 1–77 (1993).

[59] C.C. Mitchell and D.G. Schaeffer, A two–current model for the dynamics of cardiac membrane, *Bulletin math. Bio.*, 65, 767–793 (2003).

[60] M. Penicka, J. Bartuneck, B. De Bruyne, M. Vanderheyden, M. Goethals, M. De Zutter, P. Brugada, and P. Geelen, Improvement of left ventricular function after cardiac resynchronisation therapy is predicted by tissue doppler imaging echocardiography, *Journal of the american heart association* (2004).

[61] Y. Goletsis, C. Papaloukas, D.I. Fotiadis, A. Likas, and L.K. Michalis, Automated ischemic beat classification using genetic algorithms and multicriteria decision analysis, *IEEE transactions on Biomedical Engineering* (2004).

[62] M. Boulakia, M.A. Fernández, J.-F. Gerbeau, and N. Zemzemi, Towards the numerical simulation of electrocardiograms, *Functional Imaging and Modeling of the Heart, Lecture Notes in Computer Science, Springer–Verlag* , 4466, 240–249 (2007).

Section 3.5 :

[63] J. L. Berry, A. Santamarina, J. E. Moore Jr., S. Roychowdhury, and W. D. Routh, Experimental and Computational Flow Evaluation of Coronary Stents, *Annals of Biomedical Engineering*, 28, 386-398 (2000).

[64] A. I. Barakat, and E. T. Cheng, Numerical Simulation of Fluid Mechanical Distrurbance Induced by Intravascular Stents, *Proceedings of ICMMB-11 : International Conference on Mechanics in Medecine and Biology* (2000).

[65] S. Sukavaneshvar, G. M. Rosa and K. A. Solen, Enhancement of Stent-Induced Thromboembolism by Residual Stenoses, Contribution of Hemodynamics, *Annals of Biomedical Enginneering*, 28, 182-193 (2000).

[66] J. E. Moore Jr, and J. L. Berry, Fluid and Solid Mechanical Implications of Vascular Stenting,*Annals of Biomedical Engineering*, 30, 498–508 (2002).

[67] T. A. Guimaraes , M. A.V. Duarte and S. A. G. Oliveira, Topology Optimization of the Stent Cells Plane Model With Maximum Hardening and Flexibility, *Inverse Problems, Design Theory and Optimization Symposia*, ABCM, 1–8 (2004).

[68] N. Benard, Analyse de l'écoulement physiologique dans un stent coronarien : application à la caractérisation des zones de resténose pariétale, *PhD thesis*, Université de Poitiers (2005).

[69] M. C. Delfour, A. Garon and V. Longo, Modeling and Design of Coated Stents to Optimize the Effect of the Dose *SIAM Journal on Applied Mathematics*, 65(3), 858–881 (2005).

[70] Hill R., *Mathematical Theory of Plasticity*, Clarendon Press, Oxford Classic Series (1998).

Du transport de particules à l'optimisation globale sous contrainte d'équations aux dérivées partielles

Résumé : pour bien comprendre les orientations suivies dans ce mémoire, il convient de replacer les travaux présentés dans leur contexte historique. Au commencement de ce travail, au milieu des années 90, il y eut le projet de navette européenne Hermès et les problèmes associés de réentrée dans la haute atmosphère qui m'orientèrent vers l'étude des modèles cinétiques et leurs simulations numériques par les méthodes de type Monte Carlo. Malheureusement, le lancement de la fusée Ariane 5, réalisé en 1997, est à ce jour le dernier grand projet spatial européen. A la fin des années 90, avec l'essor des moyens informatiques, de nouvelles perspectives virent le jour dans les bureaux d'études d'ingénieurs : la possibilité de lancer une boucle d'optimisation en arrière plan de simulations complexes 3D : cette nouvelle voie me redirigea alors vers l'étude et l'amélioration des méthodes d'optimisation de type Algorithmes Génétiques pour toutes sortes d'applications : optimisation du Cx d'automobiles, optimisation du rendement de réacteurs d'avions, etc... Le même type de problèmes d'optimisation s'est ensuite retrouvé dans le domaine médical et a attiré mon attention depuis mon intégration au sein de l'équipe REO en 2004 : optimisation de dispositifs médicaux comme les stents ou les pacemakers, identification de paramètres de modèles numériques d'écoulements sanguins.

La première partie de ce mémoire est consacrée à des travaux sur le transport de particules dans le prolongement de ma thèse soutenue en 1995 : étude du libre parcours moyen de particules dans un réseau d'obstacles périodiques, trajectoires de particules dans un écoulement fluide turbulent. La seconde partie consiste en la présentation des méthodes d'optimisation hybrides et des principes d'évaluations approchées ayant permis d'améliorer les performances des méthodes de type Algorithmes Génétiques. La troisième partie présente un certain nombre d'application des méthodes précédentes à des problèmes d'optimisation ayant pour point commun leur caractère global ainsi que la présence de contraintes s'exprimant sous la forme d'EDO ou d'EDP. Chacun de ces problèmes est par ailleurs issu d'une problématique d'ingénierie ou médicale.

From particle trajectories to global optimization with partial differential equations constraints

Summary : in order to understand the evolution of this work throughout the years, some historical explanations are needed. At the beginning of this work, in the mid-90's, the Hermes project and its associated reentry problem, lead me to study kinetic models and their corresponding numerical simulations with the Monte Carlo method. Unfortunately, the Ariane 5 firing in 1997 is up to now the last large European space project. At the end of this decade, with the growing computational ability, a new perspective opened for engineers : the possibility to do an optimization loop even with complex 3D simulations. This new challenge brought me to the field of evolutionary algorithms in order to try to apply and eventually improve them for various problems : car shape optimization, turbine blade shape optimization etc... The same kind of problems appeared later in the medical field in which I work since 2004 and my integration inside the REO team : optimization of medical devices like stents or pacemakers, parameters identification of numerical blood flow models, etc...

The first part of this document is devoted to my work on particles transport after my PhD defence in 1995 : asymptotic behavior of the particles mean free path in a periodic array of scatterers, particles trajectories in a turbulent fluid. The second part of this document deals with the description of hybrid optimization methods and surrogate models developed in order to improve the performance of evolutionary algorithms. Finally, the third and last part gives various applications of the previous optimization methods to applicative fields, coming either from industry or medicine, and having all ODE or PDE constraints.